Computer-Aided Process Intensification of Natural gas to Methanol Process

Mohammed Sadaf Monjur and M. M. Faruque Hasan[*]

Artie McFerrin Department of Chemical Engineering, Texas A&M University

College Station, TX 77843-3122, USA.

Abstract

The recent revolution in shale gas has presented opportunities for distributed manufacturing of key commodity chemicals, such as methanol, from methane. However, the conventional methane-to-methanol process is energy intensive which negatively affects the profitability and sustainability. We report an intensified process configuration that is both economically attractive and environmentally sustainable. This flowsheet is systematically discovered using the building block-based representation and optimization methodology. The new process configuration utilizes membrane-assisted reactive separations and can have as much as 190% higher total annual profit compared to a conventional configuration. Additionally, it has 57% less CO_2-equivalent greenhouse gas (GHG) emission. Such drastic improvement highlights the advantages of building block-based computer-aided process intensification method.

Keywords: Computer Aided Process Intensification, Natural Gas Utilization, Methanol Production, Modular Process, Process Optimization.

---

[*]Correspondence should be addressed to M.M. Faruque Hasan at hasan@tamu.edu, Phone: (979) 862-1449.

Introduction

Natural gas is the cleanest fossil fuel with abundant reserves to sustain as a primary feedstock for the chemical industry. Methane is the predominant chemical species in natural gas. The availability of shale gas, which is also a form of natural gas found in shale formation,[1] presents many opportunities to the petrochemicals, chemicals, and fuel industries[2]. While the economically recoverable natural gas reservoirs started to show a declining trend,[3] and at the same time, consumption of natural gas started to increase, the emergence of horizontal drilling and hydraulic fracturing has helped shale gas extraction possible and profitable. As a result, the yearly average production of natural gas has increased 4% annually from 2005 to 2015. It was expected to have a 7% annual growth from 2018 to 2020.[4] It is estimated that almost 50% of the dry gas production will come from shale gas by 2040,[5] which will increase up to 90% in 2050[4].

Although the shale gas production has increased in recent years, lack of midstream infrastructure impedes the exploitation of shale gas resources in remote areas.[6] Much of the natural gas produced at small quantities or remote locations is flared, leading to waste of resources and increase in greenhouse gas (GHG) emission to the environment. According to the Energy Information Administration, the vented and flared natural gas increased by 225% between 2010 and 2019.[7] To this end, modular technologies are identified to have great potentials in the monetization of such unconventional resources.[8]

Methanol is one of the products that can be synthesized from shale-based natural gas. It has varied uses in a "Methanol Economy", where methanol is considered the main source for energy.[9] Methanol is a well-known energy carrier and it has better energy storage ability than hydrogen. Additionally, it can be used as an intermediate for several important chemicals (see Figure 1).[10] Global methanol demand in 2010 was 49 million metric tons (MT), which increased to 80 million MT in 2016.[11] The demand for 2021 is predicted to be 110.2 million MT[12]. The global demand for methanol is expected to grow steadily with an annual growth rate of 5.5%.[13]

Direct conversion of natural gas to chemical can be challenging as it requires different reaction conditions for breaking the C-H bond and forming new bonds to produce the end products.[14] Natural gas is often used to generate syngas, which is a predominant mixture of CO and H_2. Reforming is the most widely used technology to produce syngas at industrial scale.[15] Several technologies are available, namely steam methane reforming[16], partial oxidation (POX)[17], dry reforming[18], auto thermal reforming[19], and combined reforming[20]. The selection of appropriate reforming path for syngas generation depends on the final products, energy requirement, availability of reforming agents, and

CO_2 reduction and waste treatment targets. While many works are available for finding the appropriate reforming routes[15,21–24], few others addressed designing small-scale modular processes[25–27]. Natural-gas-to-methanol process is one of the largest energy consumers in the chemical industry.[28,29] The large energy consumption affects the profitability and sustainability. Additionally, the process is thermodynamically limited and the methanol yield of a conventional reactor is low.[30] To make the methanol synthesis process more economically attractive for small scale manufacturing, novel design solutions are needed. To improve the energy efficiency, process integration strategies can be considered.[31,32] However, they alone cannot suggest novel design solutions. To this end, process intensification is a holistic approach that seeks novel designs with significant improvements in processing volume, energy efficiency, environmental impact, and economics.[33] Several intensified reactor designs have been proposed in the literature to improve the methanol yield. They include membrane reactor[34,35] and sorption-enhanced reaction processes.[36]
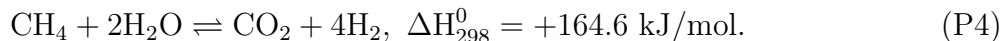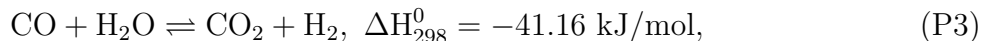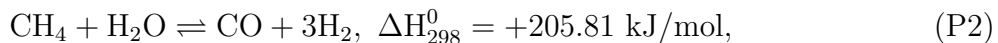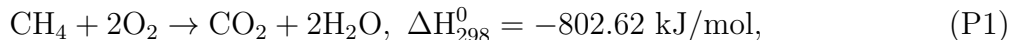
[**Figure 1 about here**]

In this work, we employ the building block[37] method for the synthesis of intensified methanol production process. In this method, various chemical and physical phenomena such as vapor-liquid equilibrium, gas permeation, reaction, etc., are represented using abstract building blocks to automatically generate and screen novel designs without pre-postulation of any candidate designs beforehand. The remainder of the article is organized as follows: First, we present a brief description of the conventional methanol process using a base-case design. Then, we discuss the building block-based approach for process synthesis and intensification. Specifically, we describe the representation methodology, mathematical model, objective functions, profitability and sustainability metrics. After that, we present and discuss the details of a novel intensified process flowsheet. Finally, we provide some concluding remarks with brief summary of the findings.

Preliminary Conceptual Design

[**Figure 2 about here**]

A conventional natural gas to methanol process is shown in Figure 2 (this flowsheet is obtained based on a previous work[24]). In this conceptual base design, POX is selected to produce syngas with a H_2:CO ratio closer to 2:1, which is suitable for methanol synthesis.[38] POX is an exothermic reaction where methane reacts with oxygen at adiabatic condition. The overall POX can be represented by the following four reactions:
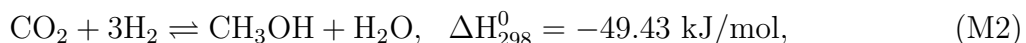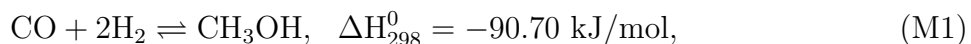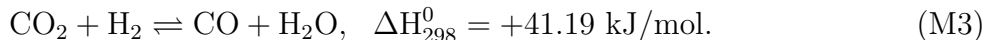
$$CH_4 + 2O_2 \rightarrow CO_2 + 2H_2O, \ \Delta H^0_{298} = -802.62 \text{ kJ/mol}, \tag{P1}$$

$$CH_4 + H_2O \rightleftharpoons CO + 3H_2, \ \Delta H^0_{298} = +205.81 \text{ kJ/mol}, \tag{P2}$$

$$CO + H_2O \rightleftharpoons CO_2 + H_2, \ \Delta H^0_{298} = -41.16 \text{ kJ/mol}, \tag{P3}$$

$$CH_4 + 2H_2O \rightleftharpoons CO_2 + 4H_2, \ \Delta H^0_{298} = +164.6 \text{ kJ/mol}. \tag{P4}$$

We assume that pure oxygen and pipeline quality natural gas (99.9% CH_4 and 0.1% H_2) are available at 300 K and 26 bar. The raw materials are heated to 773 K before they enter the POX reactor. The POX reactor is filled with Ni-Al_2O_3 catalyst, and operates adiabatically at 20 bar. Due to the exothermic nature of the POX reaction, the reactor temperature can rise up to 1573 K. The raw syngas from the POX reactor is compressed to 39 bar and then cooled to 313 K before sending it to a vapor-liquid equilibrium (VLE) separator, VLE-1, where liquids (mostly water) are separated from the syngas.

In reality, the syngas that is produced by POX has H_2 to CO ratio around 1.8. To adjust the syngas ratio and make it suitable for methanol synthesis, water gas shift (WGS) reactor is added to the process. In this reactor, CO reacts with steam at 39 bar and generates more H_2 which increases the overall syngas ratio close to 2.0:

$$CO + H_2O \rightleftharpoons CO_2 + H_2, \ \Delta H^0_{298} = -41.1 \text{ kJ/mol}. \tag{W}$$
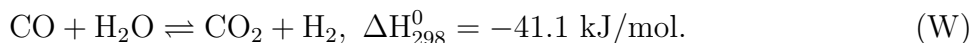
As the WGS reactor operates between 453 K$-$573 K the raw syngas from the VLE-1 separator is heated before entering the WGS reactor. Steam is compressed and heated before feeding to the WGS reactor. Note that we consider a saturated steam at 373 K and 1 bar, but slightly superheated (not saturated) steam may be adopted to avoid potential compressor damage. The product syngas from the WGS reactor is cooled to 313 K and sent to a second VLE separator (VLE-2) to remove excess water. To remove any small amount of CO_2 that may be present in the syngas, a membrane separator is used. The retentate side of the membrane is maintained at 39 bar and 313 K, whereas the permeate side has a pressure of 29 bar. After the membrane separator, the clean syngas is compressed and sent to the methanol synthesis (MeOH) reactor where the following reactions take place over $Cu-ZnO-Al_2O_3$ catalyst:

$$CO + 2H_2 \rightleftharpoons CH_3OH, \ \ \Delta H^0_{298} = -90.70 \text{ kJ/mol}, \tag{M1}$$

$$CO_2 + 3H_2 \rightleftharpoons CH_3OH + H_2O, \ \ \Delta H^0_{298} = -49.43 \text{ kJ/mol}, \tag{M2}$$

4

$$CO_2 + H_2 \rightleftharpoons CO + H_2O, \quad \Delta H_{298}^0 = +41.19 \text{ kJ/mol.} \qquad (M3)$$

Here, Eq. M1 and Eq. M2 are hydrogenation reactions that convert CO and CO_2 to CH_3OH. Eq. M3 is the reverse water-gas shift (RWGS) reaction. As the methanol synthesis reactions are favored at high pressures and low temperatures, the MeOH reactor is operated at 75 bar and $453-543$ K. The MeOH reactor products are cooled and sent to a flash separator, VLE-3, that separates the unconverted reactants from the produced methanol. As the single pass conversion of the MeOH reactor is low, 95% of the unconverted reactants are recycled back to the MeOH reactor. The liquid product that leaves the VLE-3 contains 90% (vol./vol.) methanol. To increase the purity of the product, further purification is required. However, as VLE-3 operates at a higher pressure (33 bar), significant amount of gases remain dissolved in liquid that leaves the separator. Thus, the liquids are flashed to 1 bar at VLE-4. After that, the liquids from VLE-4 are sent to a distillation column with 48 trays, which operates at 1 bar and has negligible pressure drop between the stages. The minimum purity requirement of methanol in the distillate (which is the final product) is 99.5% (vol./vol.). The column has a total-condenser that operates with a reflux ratio of 0.4 (mol basis). The feed to the distillation column enters at the 38th stage. We consider the methanol/water splitting to be performed at atmospheric condition, but a slightly higher pressure may be beneficial to avoid any vacuum in real operations.

We employ De Groote and Froment model[39] to model the POX reaction kinetics. We also consider the modification proposed by De Smet et al.[40] for the methane oxidation as it is more suited for Ni-based catalyst. The WGS kinetics is represented by the Amadeo and Laborde[41] model. Several kinetic models (e.g., Graaf et al.,[42] Slotboom et al.,[43] Lacerda et al.,[44] Bisotti et al.,[45] among others) are available for the MeOH reaction. We employ the Bussche and Froment model[46] as it shows good agreement with industrial reactor data.[47,48] The detailed reaction kinetics for all three reactions are presented in the Supporting Information (Section S5).

Process Synthesis Methodology

Building Block Representation

Building block is a novel representation method proposed by Hasan and co-workers.[37,49,50] It is based on abstract building blocks concept where each block is considered as a finite volume that can represent various fundamental phenomena common to chemical process industry (CPI). Because of this phenomena scale representation, building block can generate novel

designs without any postulation of candidate designs beforehand. For this reason, building block-based approach has been implemented to several design and synthesis problems recently.[48,51–55]

Each building block has two design elements—the block interior and the surrounding four boundaries (Figure 3a(i)). Block interior can either be empty or filled with functional elements such as catalyst or adsorbent. Temperature, pressure, and species compositions are the major attributes of each block. Based on these attributes and the thermodynamic properties of involved species, the phase of a block is determined. Multiphase systems, such as VLE, are represented using multiple blocks. Material and energy can transfer between adjacent blocks through interblock streams. Additionally, external feed streams can be introduced to and product streams can be taken out from each block which enable the interaction with the outside of the overall system. Energy can also be supplied to and taken out from each block by external utility.

The interaction between adjacent blocks are described by the common boundaries in between. Depending on the types of flow across the boundary, block boundaries can be of three types: (i) unrestricted, (ii) semi-restricted, and (iii) completely restricted (Figure 3a(ii)). An unrestricted boundary indicates that the flow through the boundary is not subjected to any kind of restriction and does not affect the stream compositions. A semi-restricted boundary changes the stream composition from the source block composition. This type of boundary indicates the presence of a mass transfer interceptor, for example, a barrier material such as a membrane. A semi-restricted boundary may also represent the interface of a multiphase system. Lastly, a completely restricted boundary prohibits any flow through the boundary often representing the wall of an equipment.

Combining these features of block internal and boundaries in various manners, many physicochemical phenomena can be modeled (Figure 3b). Complete mixing and splitting of same-phase streams are modeled with single blocks with multiple inlets and outlets. Heating and cooling are represented through heaters and coolers located at the unrestricted block boundaries. Similarly, pressure change is represented by pressure manipulators (e.g., compressors, turbines, pumps, and JT valves) positioned at unrestricted block boundaries. Chemical reactions take place inside a block when the block interior is filled with catalysts. Separation phenomena are represented by two blocks sharing a common semi-restricted boundary. For example, vapor-liquid phase contact is depicted in Figure 3b(vi). Here, the left block is in liquid phase and the right block is in vapor phase. The semi-restricted boundary separating the two blocks mimics the phase contact and the interblock flow through the phase boundary is governed by phase equilibrium. Similarly, when the semi-restricted boundary is assigned with a membrane material, we mimic all types of membrane operations including gas

permeation (Figure 3b(vii)), pervaporation (Figure 3b(viii)), and liquid permeation (Figure 3b(ix)). Mass transfer through the semi-restricted boundaries are determined by imposing appropriate governing laws (e.g., Fick's law or Darcy's law).

[**Figure 3 about here**]

By combining these phenomena representation blocks, we can create or mimic many unit operations. A few examples are shown in Figure 3c. When a single block is used to represent the reaction phenomena, it represents a continuous stirred tank reactor (CSTR). However, to capture the behaviour of a conventional plug flow reactor (PFR), we need multiple catalyst carrying blocks positioned in series (Figure 3c(i)). Similarly, to represent a membrane reactor we need two rows of blocks separated by a common membrane material. Figure 3c(ii) depicts one such membrane reactor where the blocks in the second row (yellow blocks) represent the reactor side and the blocks in the first row (white blocks) represent the permeate side. VLE separators and membrane separators each require two blocks, as shown in Figures 3c(iii) and 3c(iv), respectively. To represent a distillation column, multiple block pairs in series are required. Each of the block pairs must have a common semi-restricted boundary to represent the VLE phase contact. When several blocks are arranged in a two-dimensional grid, we get a process superstructure with all plausible equipment and their connectivities, which can used to generate numerous intensified and nonintensified process flowsheets.

The applicability and rigorousness of building block representation can be illustrated using an n-CSTRs in series model for packed bed reactors. As we use more blocks, we capture the phenomena behavior more accurately. To illustrate, we have simulated a number of reactors using the building block and a commercial process simulator Aspen Plus v11. Namely, we use single block, 3 blocks and 10 blocks in series to represent the reactor. Figure 4a represents CH_4 conversion in POX reactor for different amounts of the catalyst. The blue line represents the conversion of a single block, while the yellow line represents the conversion of a CSTR simulated in Aspen Plus. As these two lines are overlapping, we can safely claim that a single building block is able to replicate a CSTR. The top red line represents the conversion of a kinetic PFR simulated in Aspen Plus. As shown in Figure 4a, with the increasing number of reactor building blocks, the conversion of a PFR approaches to that of the Aspen Plus-based PFR. As a PFR can be exactly represented using infinite number of CSTR arranged in series, if large number of blocks are used, the building block conversion eventually matches the Aspen Plus conversion. However, this makes the model computationally more time-intensive.

[**Figure 4 about here**]

Figure 4b shows the relative accuracy gaps between the Aspen Plus & the building block-based PFR simulation and the required simulation times (in seconds) for each n-block-CSTR. With the increasing number of blocks, the relative gap reduces and the building block-based model prediction becomes more accurate. However, the simulation time also increases significantly. For instance, when 30 blocks are used for PFR representation, the simulation accuracy is >99%, but the required simulation time is in the order of minutes. Upon considering the tread-offs between model accuracy and size, we decide to use 10 blocks for PFR representation as both the accuracy and simulation time are reasonable. We performed similar studies for WGS reactors and found that about ten building blocks are sufficient to represent the WGS reactor (Figure 4c) and the MeOH reactor (Figure 4d).

The building block superstructure and the associated model described above is applicable to general process synthesis problems. However, one would benefit from tailoring it to specific case where the phenomena are known. The conceptual base design of methanol process can be represented as shown in Figure 3d. Here, we considered two separate superstructures. In the first superstructure (Figure 3d(i)), we stack 70 blocks in 5 rows and 14 columns and it captures the process up VLE-3. Let $B_{i,j}$ denote the block in row i and column j. $B_{1,1}$ is the feed block, where both natural gas and oxygen are introduced. The POX reactor is positioned using ten blocks in series between $B_{1,2}$ to $B_{1,11}$ (light green blocks). The first VLE separator (VLE-1) is represented by blocks $B_{1,13}$ and $B_{1,14}$ (light blue blocks), where the thick vertical blue line between the blocks represents the vapor-liquid interface. As syngas enters VLE-1 in vapor phase, we fix the phase of block $B_{1,13}$ to vapor and block $B_{1,14}$ to liquid. Steam for WGS reaction enters the process at block $B_{2,14}$, where it is compressed and heated to the temperature and pressure of WGS reactor. The steam along with the syngas from VLE-1 enters the WGS reactor at block $B_{2,11}$, which is a PFR represented by ten blocks positioned from block $B_{2,11}$ to block $B_{2,2}$ (light yellow blocks). VLE-2 is represented by block $B_{3,1}$ (vapor phase) and block $B_{4,1}$ (liquid phase). The vapor stream leaving the VLE-2 enters the CO_2 separator at block $B_{3,5}$. The CO_2 separator is presented by six blocks, block $B_{3,3}$ to block $B_{3,5}$ and block $B_{4,3}$ to block $B_{4,5}$ (golden blocks). Here, the blocks $B_{3,3}$ to $B_{3,5}$ represent the retentate side, the blocks $B_{4,3}$ to $B_{4,5}$ represent the permeate side, and the green thick horizontal line represents the membrane material. The flow direction in the permeate side is considered to be counter-current. The permeate (CO_2 stream) leaves the process as waste from block $B_{4,3}$. The MeOH reactor is represented by the orange blocks ($B_{3,9}$–$B_{3,14}$, $B_{4,13}$, $B_{4,14}$, $B_{5,13}$, and $B_{4,14}$). VLE-3 is represented by blocks $B_{5,9}$ (vapor phase) and $B_{5,10}$ (liquid phase). Liquid methanol leaves from block $B_{5,10}$ as a crude product, whereas the vapor stream leaves VLE-3 from block $B_{5,9}$. The purge stream is taken out from block $B_{5,8}$ and the remaining unreacted reactants are recycled back to the MeOH reactor using

the recycle blocks ($B_{5,7}$, $B_{5,6}$ and $B_{4,6}$). The heat exchanger in the recycle line is modeled by allowing heat exchange between block $B_{5,6}$ and block $B_{4,11}$. Here, block $B_{5,6}$ represents the hot side of the heat exchanger, that discards heat and block $B_{4,11}$ depicts the cold side, that receives the discarded heat. Details of this heat exchanger model can be found in the Supporting Information (see Section S3). VLE-4 and distillation column is modelled in a 50×4 superstructure shown in Figure 3d(ii). Here, the liquid crude methanol product that leaves the first superstructure from block $B_{5,10}$ enters as feed at block $B_{1,4}$. The VLE-4 is presented by blocks $B_{2,4}$ and $B_{2,3}$, where the phase of the first block is liquid and the later one is vapor. The gases from the VLE-4 leaves from block $B_{2,3}$ as purge. The liquid from block $B_{2,4}$ leaves as jump outlet (black downward arrow) and enters to the distillation column at block $B_{39,2}$ as jump inlet (purple downward arrow). The 48 stage distillation column along with the condenser and re-boiler is represented by 50 block pairs of first ($j = 1$) and second columns ($j = 2$). Here, all the blocks in the first column are in vapor phase and the blocks in the second column is in liquid phase. The block pair in first row (i.e., $B_{1,1}$ and $B_{1,2}$) represents the total condenser. The distillate leaves the distillation column from block $B_{1,2}$. The partial re-boiler is located at the 50th row from where the bottom product is taken out.

Eventually, the generic representation using building blocks would allow us to construct a general process superstructure with all plausible alternative flowsheet configurations embedded within using a collection of blocks arranged in a two-dimensional grid.

Model Formulation

We now describe a model that describes the overall process superstructure. Every block in the superstructure is designated as $B_{i,j}$ where, $i \in \mathcal{I} = \{1, ..., |\mathcal{I}|\}$ is the row number and $j \in \mathcal{J} = \{1, ..., |\mathcal{J}|\}$ is the column number. Temperature, pressure, and composition of chemical at each block are expressed as $T_{i,j}$, $P_{i,j}$, and $y_{i,j,k}$, respectively. $F_{i,j,k}$ and $R_{i,j,k}$ define flow rates of component k that enters block $B_{i,j}$ from the horizontal and vertical direction, respectively. $M_{i,j,k,f}$ and $N_{i,j,k,p}$ defines the component flow rates to and from block $B_{i,j}$ in feed stream f and in product stream p, respectively. $G_{i,j,k}$ defines the generation and/or consumption of component k due to chemical reactions in block $B_{i,j}$. Additionally, to increase the connectivity between nonadjacent blocks, we allow "jump flows", $J_{i,j,i',j',k}$ where the flow direction of component k is from block $B_{i,j}$ to block $B_{i',j'}$.

The model is formulated based on several sets. The set $\mathcal{K} = \{k|k = 1, ..., |\mathcal{K}|\}$ represents the set of chemical components, $\mathcal{F} = \{f|f = 1, ..., |\mathcal{F}|\}$ denotes the set of available raw materials, and $\mathcal{P} = \{p|p = 1, ..., |\mathcal{P}|\}$ denotes the set of specified products. The set of chemical reactions is $\mathcal{R} = \{r|r = 1, ..., |\mathcal{R}|\}$. We also define $\mathcal{C} = \{c|c = 1, ..., |\mathcal{C}|\}$ as the set

9

of available catalysts. The set of separation phenomena is denoted by $\mathcal{S} = \{s|s = 1, ..., |\mathcal{S}|\}$ and the set of enabling materials is represented by $\mathcal{M} = \{m|m = 1, ..., |\mathcal{M}|\}$. The original building block-based model[37] was formulated as a mixed-integer nonlinear program (MINLP) with several disjunctions used for deciding the position of the active phenomena, block phase, flow direction, etc. In this work, to reduce the computational burden, we replace the disjunctive terms by subsets to fix flow directions, block phases, and phenomena. However, binary variables are still in use to decide whether the allowed phenomena are active or not. The general equations are summarized as follows:

$$F_{i,j-1,k} + R_{i-1,j,k} - F_{i,j,k} - R_{i,j,k} + \sum_{f \in \mathcal{F}} M_{i,j,k,f} - \sum_{p \in \mathcal{P}} N_{i,j,k,p} + \sum_{(i',j') \in Link} J_{i',j',i,j,k}$$
$$- \sum_{(i',j') \in Link} J_{i,j,i',j',k} = 0, \quad (i,j) \in ActB/RxnB, k \in \mathcal{K}, \tag{1}$$

$$F_{i,j-1,k} + R_{i-1,j,k} - F_{i,j,k} - R_{i,j,k} + G_{i,j,k} + \sum_{(i',j') \in Link} J_{i',j',i,j,k} = 0, \quad (i,j) \in RxnB, k \in \mathcal{K}, \tag{2}$$

$$G_{i,j,k} = f^{rxn}(T_{i,j}, P_{i,j}, y_{i,j,k}, k_r^0, E_r^A, V_{i,j,c}, \tau_r, z_{i,j,c}^{rxn}), \quad (i,j) \in RxnB, k \in \mathcal{K}, \tag{3}$$

$$F_{i,j,k} = FP_{i,j,k} - FN_{i,j,k}, \quad (i,j) \in ActF, k \in \mathcal{K},$$
$$R_{i,j,k} = RP_{i,j,k} - RN_{i,j,k}, \quad (i,j) \in ActR, k \in \mathcal{K}, \tag{4}$$

$$y_{k,p}^{min,prod} \sum_{k' \in \mathcal{K}} N_{i,j,k',p} \leq N_{i,j,k,p}, \quad i \in \mathcal{I}, j \in \mathcal{J}, (k,p) \in KP, \tag{5}$$

$$FP_{i,j,k} = y_{i,j,k} \sum_{k' \in \mathcal{K}} FP_{i,j,k'}, \quad (i,j) \in UnFP, k \in \mathcal{K},$$
$$FN_{i,j,k} = y_{i,j+1,k} \sum_{k' \in \mathcal{K}} FN_{i,j,k'}, \quad (i,j) \in UnFN, k \in \mathcal{K},$$
$$RP_{i,j,k} = y_{i,j,k} \sum_{k' \in \mathcal{K}} RP_{i,j,k'}, \quad (i,j) \in UnRP, k \in \mathcal{K}, \tag{6}$$
$$RN_{i,j,k} = y_{i+1,j,k} \sum_{k' \in \mathcal{K}} RN_{i,j,k'}, \quad (i,j) \in UnRN, k \in \mathcal{K},$$

$$N_{i,j,k,p} = y_{i,j,k} \sum_{k' \in \mathcal{K}} N_{i,j,k',p}, \quad (i,j,p) \in ProdB, k \in \mathcal{K}, \tag{7}$$

$$J_{i,j,i',j',k} = y_{i,j,k} \sum_{k' \in \mathcal{K}} J_{i,j,i',j',k'}, \quad (i,j,i',j') \in Link, k \in \mathcal{K}, \tag{8}$$

$$\sum_{k \in \mathcal{K}} y_{i,j,k} = 1, \quad (i,j) \in ActB, \tag{9}$$

$$y_{i,j,k} = K^{eq}_{i,j,k,s,m} y_{i,j+1,k}, \quad (i,j) \in VLEF, k \in \mathcal{K}, (s,m) \in Equil, \tag{10a}$$

$$y_{i,j,k} = K^{eq}_{i,j,k,s,m} y_{i,j-1,k}, \quad (i,j) \in VLEF, k \in \mathcal{K}, (s,m) \in Equil, \tag{10b}$$

$$y_{i,j,k} = K^{eq}_{i,j,k,s,m} y_{i+1,j,k}, \quad (i,j) \in VLER, k \in \mathcal{K}, (s,m) \in Equil, \tag{11a}$$

$$y_{i,j,k} = K^{eq}_{i,j,k,s,m} y_{i-1,j,k}, \quad (i,j) \in VLER, k \in \mathcal{K}, (s,m) \in Equil, \tag{11b}$$

$$K^{eq}_{i,j,k,s,m} = f^{VLE}(T_{i,j}, P_{i,j}), \quad (i,j) \in VLE, k \in \mathcal{K}, (s,m) \in Equil, \tag{12}$$

$$P_{i,j} \geq P^{bub}_{i,j}, \quad (i,j) \in LB; \quad P_{i,j} \leq P^{dew}_{i,j}, \quad (i,j) \in VB^{chk}, \tag{13}$$

$$R_{i,j,k} = \sigma_{k,s,m} \left(\sqrt{P_{i,j} y_{i,j,k}} - \sqrt{P_{i+1,j} y_{i+1,j,k}} \right) A_{i,j,s,m}, \quad (i,j) \in MemB, k \in \mathcal{K}, (s,m) \in R1, \tag{14}$$

$$R_{i,j,k} = \lambda_{k,s,m} (P_{i,j} y_{i,j,k} - P_{i+1,j} y_{i+1,j,k}) A_{i,j,s,m}, \quad (i,j) \in MemB, k \in \mathcal{K}, (s,m) \in R2, \tag{15}$$

$$A_{i,j,s,m} \leq A^{max}_m z^{sR}_{i,j,s,m}, \quad (i,j) \in MemB, (s,m) \in Rate, \tag{16}$$

$$\begin{aligned} EF_{i,j-1} + ER_{i-1,j} - EF_{i,j} - ER_{i,j} + EJ^f_{i,j} - EJ^p_{i,j} + EM_{i,j} - EN_{i,j} \\ + W^{comp}_{i,j} - W^{exp}_{i,j} + Q^h_{i,j} - Q^c_{i,j} = 0, \quad (i,j) \in ActB/RxnB, \end{aligned} \tag{17}$$

$$EF_{i,j-1} + ER_{i-1,j} - EF_{i,j} - ER_{i,j} + EJ^f_{i,j} + EG_{i,j} + W^{comp}_{i,j} - W^{exp}_{i,j} = 0, \quad (i,j) \in POX, \tag{18}$$

$$\begin{aligned} EF_{i,j-1} + ER_{i-1,j} - EF_{i,j} - ER_{i,j} + EG_{i,j} + W^{comp}_{i,j} - W^{exp}_{i,j} \\ + Q^h_{i,j} - Q^c_{i,j} = 0, \quad (i,j) \in WGS \cup MeOH, \end{aligned} \tag{19}$$

$$\begin{aligned} Q^h_{i,j} = \sum_{(i',j')} q^{hex}_{i',j',i,j}(q^{hex,UP}_{i',j',i,j}, z^{hex}_{i',j',i,j}), \quad (i'j',i,j) \in Hx, (i,j) \in CB, \\ Q^c_{i,j} = \sum_{(i',j')} q^{hex}_{i,j,i',j'}(q^{hex,UP}_{i,j,i',j'}, z^{hex}_{i,j,i',j'}), \quad (i,j,i',j') \in Hx, (i,j) \in HB, \end{aligned} \tag{20}$$

$$\mathbf{g}(T_{i,j}, P_{i,j}, V_{i,j,c}, A_{i,j,s,m}, z^{rxn}_{i,j,c}, z^{sR}_{i,j,s,m}) \leq 0. \tag{21}$$

Eq. 1 represents the material balance for non-reactive blocks, whereas Eq. 2 represents the material balance for reactive blocks. $ActB$ designates the set of active blocks within

the superstructure. $RxnB$ is a subset of $ActB$ and refers to the reactor blocks. Segregation of the pre-specified reactive blocks from the non-reactive blocks significantly reduces the model complexity. Eq. 3 describes the consumption/generation of components ($G_{i,j,k}$) due to chemical reactions from block temperature; pressure; component composition; pre-exponential factor (k_r^0), activation energy (E_r^A), effectiveness factor (τ_r) of reaction r; and amount ($V_{i,j,c}$) of catalyst c. Here, binary variable $z_{i,j,c}^{rxn}$ indicates the presence of catalyst c in block $B_{i,j}$. Flow rates in the horizontal and vertical directions are calculated by Eq. 4, where sets $ActF$ and $ActR$ designate the blocks where these equations are active. Eq. 5 ensures the specified minimum purity of component k in product stream p given by $y_{k,p}^{min,prod}$. The compositions of all the streams that are leaving from a block through unrestricted boundaries have to be equal to the compositions of the source block. This constraint is imposed by Eq. 6. Here, $UnFP$ is the set of blocks where positive horizontal flow, $FP_{i,j,k}$, is allowed. On the other hand, blocks with negative horizontal flow, $FN_{i,j,k}$, are designated by the set $UnFN$. Similarly, $UnRP$ and $UnRN$ are the set of blocks where vertical flows are allowed in positive ($RP_{i,j,k}$) and negative ($RN_{i,j,k}$) directions, respectively. Eqs. 7 and 8 ensure similar constraints for products and jump outlet streams. Here, $ProdB$ is the set of blocks from where product p leaves the superstructure. The set $Link$ allows the jump flows between blocks $B_{i,j}$ and $B_{i',j'}$. Eq. 9 ensures that the summation of component mole fractions in active blocks is equal to one. The VLE compositions of each block separated by a semi-restricted boundary are determined by Eqs. 10–11. Here, $K_{i,j,k,s,m}^{eq}$ is the phase equilibrium constant which is determined by Eq. 12. When the vapor block is positioned at the left hand side and the liquid block is located at the right hand side of a semi-restricted boundary, Eq. 10a is used to estimate the compositions of these horizontal block pairs. When the block phase are interchanged, Eq. 10b is used. Similarly, Eqs. 11a–b, calculate the equilibrium composition of the vertical block pairs. The sets $VLEF$ and $VLER$ denote the blocks where these equilibrium relations are allowed and set $VLE = VLEF \cup VLER$. Eq. 13 determines the phase of a block based on the bubble and dew pressures, where LB and VB denote the set of liquid and vapor blocks, respectively. The set VB^{chk} is a subset of VB where the phase check is performed. Two different rate-based models for membrane separation are presented in Eqs. 14 and 15, where $R1$ and $R2$ are the sets of separation-material (s, m) pairs that are compatible. Here, membrane-based separation is only allowed between vertical block pairs (i.e., $B_{i,j}$ and $B_{i+1,j}$). Eq. 14 determines the flow rate $R_{i,j,k}$ through the membrane from the permeation flux ($\sigma_{k,s,m}(\sqrt{P_{i,j}y_{i,j,k}} - \sqrt{P_{i+1,j}y_{i+1,j,k}})$) and membrane surface area ($A_{i,j,s,m}$). Here, $\sigma_{k,s,m}$ is the linear slope used for determining the permeation flux. On the other hand, in Eq. 15, membrane permeance ($\lambda_{k,s,m}$) is used to estimate the flow across the membrane. In Eq. 16, A_m^{max} is the maximum allowable membrane area in each block and $z_{i,j,s,m}^{sR}$ is a

binary variable. When $z_{i,j,s,m}^{sR}$ equals to 1, membrane m is allowed to be present at block $B_{i,j}$. Set $Rate$ is the union set of $R1$ and $R2$, i.e., $Rate = R1 \cup R2$. Energy balance for non-reactive blocks are presented in Eq. 17. Eq. 18 presents the energy balance constraints for the POX reactor blocks where external heating ($Q_{i,j}^h$) or cooling ($Q_{i,j}^c$) is not allowed as the reactor operates at adiabatic condition. Energy balances for the WGS and MeOH reactor blocks are presented in Eq. 19. Here, POX, WGS, and $MeOH$ are the subsets of $RxnB$. In the energy balance equations, $EF_{i,j}$, $ER_{i,j}$, $EJ_{i,j}^f$, $EJ_{i,j}^p$, $EM_{i,j}$, $EN_{i,j}$, $EG_{i,j}$ stands for enthalpies of horizontal, vertical, jump inlet, jump outlet, feed, product streams and energy consumed or generated due to chemical reactions, respectively. $W_{i,j}^{comp}$ and $W_{i,j}^{exp}$ denotes the compression and expansion work that is added or taken out from block $B_{i,j}$, respectively. Eq. 20 represents the heat integration model. When the binary variable $z_{i,j,i',j'}^{hex}$ equals to 1, heat is allowed to transfer from a hot block $B_{i,j}$ to a cold block $B_{i',j'}$, where $q_{i,j,i',j'}^{hex}$ is the heat transfer amount. Sets HB and CB denotes the position of these hot and cold blocks within the superstructure and set $Hx_{i,j,i',j'}$ allows the heat transfer between selected block pairs. The detailed formulation of the heat integration model is provided in Section S3 of the Supporting Information.

The model includes several process and equipment specific constraints which are denoted by Eq. 21 using a general expression $\mathbf{g}(T_{i,j}, P_{i,j}, V_{i,j,c}, A_{i,j,s,m}, z_{i,j,c}^{rxn}, z_{i,j,s,m}^{sR}) \leq 0$. Detailed formulation of these constraints can be found in the Section S2 of Supporting Information (Eqs. S7–S13, S21–S26) along with the detailed explanations and formulation of the overall model. Additionally, the definition of sets, indices, variables, and parameters are listed in Section S1 of the Supporting Information.

Design Objectives

Economic Metrics

The economic objective function involves the maximization of the total annual profit (TAP) of the methanol production process. With this, the overall process synthesis is formulated as the following optimization problem:

$$\max \quad TAP = AI - TAC \tag{22}$$

$$\text{s.t. Eqs. 1--21}$$

$$TAC = AOC + AIC \tag{23}$$

$$AI = t^{opt} \sum_{(i,j,p) \in ProdB} \sum_{k \in \mathcal{K}} SP_{k,p} N_{i,j,k,p} \tag{24}$$

$$AOC = t^{opt} \times \left(\sum_{(i,j,f) \in FeedB} UC^f \sum_{k \in \mathcal{K}} M_{i,j,k,f} + \frac{UC^{elec}}{\eta_c} \sum_{(i,j) \in ActB} W_{i,j}^{comp} \right.$$
$$\left. + UC^{cu} \sum_{(i,j) \in ActB \backslash HB} Q_{i,j}^c + UC^{hu} \sum_{(i,j) \in ActB \backslash CB} Q_{i,j}^h \right) \tag{25}$$

$$AIC = CRF \times FCI + AMC \tag{26}$$

$$CRF = \frac{i \times (1+i)^N}{(1+i)^N - 1} \tag{27}$$

$$FCI = \sum_{e \in \mathcal{E}} TIC_e \tag{28}$$

$$TIC_e = C_e \left(\frac{S_e}{S_e^{ref}} \right)^{n_e} \tag{29}$$

The TAP is obtained after subtracting the total annual cost (TAC) from the annual income, AI (Eq. 22). The TAC is the summation of the annual operating cost (AOC) and the annualized investment cost (AIC) and is estimated by Eq. 23. Eq. 24 calculates the AI from the sales of methanol. Here, t^{opt} represents the yearly operating time in seconds considering 330 days of annual operation. AOC in Eq. 25 is computed as the summation of the raw material cost (first term), the electricity consumption cost to operate the rotating equipment (second term), and the cold and hot utility costs (third and fourth terms, respectively). $FeedB$ is the set of blocks where feed stream f is introduced. UC^f, UC^{elec}, UC^{cu}, UC^{hu} are the unit costs of the fresh raw materials, electricity, cold and hot utility, respectively and $SP_{k,p}$ is the sales price of methanol. The cost of natural gas, pure oxygen (stored oxygen), and steam are taken as \$2.8/kmol, \$3.5/kmol, \$0.09/kmol, respectively. Cold and hot utilities and electricity prices are considered to be \$1.9/GJ, \$3.8/GJ, and \$14/GJ, respectively. Finally, the selling price of 99.5% (vol./vol.) pure methanol is assumed to be \$400/ton. All of these values are taken from Alsuhaibani et al.[56] Eq. 26 calculates the AIC from the fixed capital investment (FCI) and the annual maintenance cost (AMC). The capital recovery factor, CRF, is calculated by Eq. 27, where i is the interest rate and N is the duration of the economic analysis (in years).[57] The AMC is considered to be 5% of FCI. Eq. 28 estimates the FCI by summing the total installed cost (TIC_e) of each equipment e. The equipment set $\mathcal{E}$ includes, reactor, compressor, heater,

cooler, heat exchanger, VLE separator, and distillation column. TIC_e is calculated from Eq. 29, where C_e is the reference installation cost, n_e is the scaling factor, S_e^{ref} is the reference size, and S_e is the scaling parameter for equipment e. The values of these cost parameters are tabulated in Table 1. Detailed formulation of these cost functions are presented in Section S8 of the Supporting Information. The TIC of a membrane reactor is considered as a weighted sum of the reactor and the membrane costs, $TIC_{membrane\,reactor} = \omega_{reactor} \times TIC_{reactor} + \omega_{membrane} \times TIC_{membrane}$. Here, $\omega_{reactor}$ and $\omega_{membrane}$ are the weight factors. In this study, we consider both $\omega_{reactor}$ and $\omega_{membrane}$ to be one.

[**Table 1 about here**]

With these constraints (Eqs. 1–29), the goal is to select:

(i) the appropriate reactors (POX, WGS, MeOH),

(ii) the reactor type (conventional/intensified/partially intensified),

(iii) the separators (membrane separator and VLE separators),

(iv) the operating conditions, and

(v) the optimal number of trays, reflux ratio, and feed entry stage of the distillation column,

in such a manner that the TAP of the process is maximized.

To assess the profitability of the process, we also compute the return on investment (ROI) as follows:

$$ROI = \frac{(AI - AOC - depreciation) \times (1 - \theta) + depreciation}{TCI} \tag{30}$$

We have adopted a 10-year linear depreciation scheme with a salvage value equal to 10% of the FCI. Additionally, the tax rate (θ) is assumed to be 30%. The total capital investment (TCI) is the summation of the FCI and the working capital investment (WCI), and we have considered WCI to be 15% of the TCI.

Sustainability Metrics

The methanol synthesis process has several indirect and direct sources of CO_2 emission. The sustainability of the process can be assessed by calculating the CO_2-equivalent GHG emissions by the following equation:

$$e^{CO_2} = \frac{\alpha^{elec}}{\eta_c} \sum_{(i,j)\in ActB} W_{i,j}^{comp} + \alpha^{fuel} \sum_{(i,j)\in ActB/CB} Q_{i,j}^h + \sum_{(i,j,f)\in FeedB} \sum_{k\in\mathcal{K}} \alpha_f^{feed} M_{i,j,k,f}$$
$$+ \sum_{(i,j,p)\in ProdB} N_{i,j,k=CO_2,p} \tag{31}$$

Here, the first term designates the indirect CO_2-equivalent emission from electricity consumption and α^{elec} is the CO_2 emission in terms of kg per MJ electricity. The second term estimates the indirect CO_2-equivalent emission from burning fuels to supply the hot utilities. The CO_2 emission per unit hot utility is designated by α^{fuel}. The third term calculates the indirect CO_2-equivalent emission from pre-processing the raw materials, which includes the processing of shale gas to produce pipeline quality natural gas and cryogenic separation of air to produce pure oxygen. We assume that the pure oxygen (stored oxygen) that is consumed as raw material is produced by cryogenic separation of air. α_f^{feed} stands for the CO_2 emission per unit amount of consumed raw material, f. The fourth term calculates the direct CO_2 emission from all products.

Methanol Process Synthesis Specification

[**Figure 5 about here**]

To incorporate process intensification and heat integration, we consider two superstructures. The 7×20 superstructure of Figure 5a produces crude methanol with 90–95% (vol./vol.) purity. In this case, the POX and the MeOH reactors can either be conventional reactors or membrane reactors. POX reactor blocks are located in the superstructure from block $B_{3,5}$ to block $B_{3,14}$ and from block $B_{2,5}$ to block $B_{2,14}$, where the blocks in the third row ($i = 3$) represents the reactor side and the blocks in the second row ($i = 2$) represents potential shell side of the reactor. Apart from the natural gas and oxygen, air and steam can also be used as feed in the POX reactor, which enter the superstructure in blocks $B_{3,1}$, $B_{1,1}$, $B_{2,1}$, and $B_{4,1}$, respectively. Additionally, heat integration is allowed between these feed streams and the POX reactor outlet stream (see Section S4 in the Supporting Information). The WGS reactor is positioned from block $B_{4,20}$ to block $B_{4,11}$ and the CO_2 separator blocks are represented by the six golden blocks ($B_{5,5}$ to $B_{5,3}$ and $B_{6,5}$ to $B_{6,3}$). The MeOH membrane reactor is represented by block $B_{5,8}$ to block $B_{5,17}$ (reactor side) and block $B_{6,8}$ to block $B_{6,17}$ (permeate side). To enhance the separation, air can be used as a sweep gas, which enters at block $B_{6,17}$. The VLE separators are denoted by the light blue blocks. An additional VLE separator (represented by block $B_{1,8}$ and block $B_{1,9}$) is considered to separate methanol from the sweep air, from the permeate side of the

MeOH membrane reactor. Jump flows are allowed for selected block pairs (please see Section S4 in the Supporting Information for more details). For instance, stream can leave block $B_{3,20}$ through a jump outlet (black downward arrow) and can enter to block $B_{4,10}$ by a jump inlet (purple downward arrow). This jump connection can acts as a bypass for the WGS reactor. The selection of semi-restricted boundaries are modeled as discrete decisions (see Section S2 in the Supporting Information). For producing 99.5% (vol./vol.) pure methanol by distillation, a 50×4 superstructure is considered, similar to the superstructure discussed in Figure 5b. Here, the two crude methanol products of the first superstructure, Crude-1 and Crude-2 enters as a feed in block $B_{1,3}$ and $B_{1,4}$, respectively. Blocks $B_{3,3}$ and $B_{3,4}$ depicts the low pressure VLE separator that separates the gases. The liquid from this VLE separator can enter any stages of the distillation column as a jump inlet. Additionally, the number of trays in the distillation column is also a decision variable. The appropriate number of tray is find by varying the number of trays between 15 to 50.

Our goal is to design a process with a utilization capacity of 214.5 mol/s of natural gas. Oxygen, steam, and air are available at a maximum flow rate of 285 mol/s, 120 mol/s, and 1200 mol/s, respectively. However, the selection of the optimal flow rate of these raw materials is a decision variable. Natural gas and oxygen are available at 300 K and 26 bar. Steam is also available at 373 K and 1 bar. Air is available at atmospheric condition (300 K and 1 bar). The temperature and pressure of the entire process are bounded between 300–1573 K and 1–77 bar, respectively. The POX reactor must operate between 773–1573 K and 20–40 bar. The WGS reactor temperature is bounded between 453–573 K. The operating temperature of the MeOH reactor must be in between 543 and 453 K, respectively. Additionally, the pressure of this reactor can vary between 40 and 77 bar. The POX membrane has a maximum allowable temperature of 1173 K.[58] For the CO_2 membrane, the maximum temperature is 313 K.[59] The MeOH membrane has a maximum allowable temperature of 543 K. For the POX membrane, the retentate and the permeate blocks should select equal pressures. For the CO_2 membrane, the maximum pressure difference across the membrane is considered to be 10 bar. However, for the MeOH membrane, no constraint on pressure difference across membrane is applied. In other word, the permeate side pressure can be the lowest allowable pressure of 1 bar, whereas the retentate side can be at 77 bar (upper bound of the pressure). Each of the POX blocks can contain at most 705 kg of catalyst. For WGS and MeOH reactor blocks, this upper limit is 1000 kg and 1504 kg, respectively. The maximum amount of catalyst that each of the POX and the MeOH reactor blocks can accommodate is estimated based on a previous study.[48] The maximum membrane surface area for the POX membrane, the CO_2 membrane, and the MeOH membrane are 94.25 m²/block, 100 m²/block, and 163.35 m²/block, respectively. These maximum membrane

surface areas for membranes are estimated based on the reactor geometry. The membrane permeance data[58–60] are provided in the Supporting Information (Section S6). The cold utility is considered to be available at 298 K which can reduce the temperature of any stream up to 300 K. Similarly, it is considered that the hot utility can increase the temperature of any stream up to 773 K. However, the temperature of a block can rise above 773 K when exothermic reactions are involved or when the block exchanges heat with another block. For instance, the temperature in the POX reactor blocks can go beyond 773 K due to the exothermic reactions. Similarly, the feed blocks can have temperature above 773 K as these blocks can exchange heat with reactor outlet blocks. To restrict unreasonably high recycle flow rates, we impose, recycle ratio ≤ 3.76,[61] where recycle ratio is the ratio between the recycle flow rates to the fresh syngas flow rates. While estimating the CRF, the interest rate is assumed to be 10% and the economic analysis is performed for 20 years. Generally, the life time of a shale gas well varies between 3 to 5 years. However, we consider that the small scale modular process is easily transportable to other locations of shale wells once one shale wells is depleted. We have not considered any additional cost for dismantling, transporting, and remounting the modular plant. All costs are converted to 2020 values by using the chemical engineering plant cost index (CEPCI). CEPCI for 2020 is taken as 668[62] whereas CEPCI of the earlier years are obtained from http://www.chemengonline.com/pci. We also assumed α^{elec} to be 0.217 kg CO_2-eqv/MJ electricity[23], α^{fuel} to be 0.039 kg CO_2-eqv/MJ hot utility[63], α^{feed}_{NG} to be 0.002 kg CO_2-eqv/mol CH_4[64], and $\alpha^{feed}_{O_2}$ to be 0.005 kg CO_2-eqv/mol O_2, considering 200 kWh energy consumption for producing each ton of O_2.[65]

We specify the following sets when optimizing the base design with 5×14 blocks: $k \in \mathcal{K} = \{CH_4, O_2, H_2, CO, CO_2, H_2O, CH_3OH\}$, $f \in \mathcal{F} = \{NG, Oxy, Steam\}$, $p \in \mathcal{P} = \{Crude, Gas\text{-}1, Liquid, Purge\}$, $s \in \mathcal{S} = \{VLPC, GP\}$, $m \in \mathcal{M} = \{VLI, CM\}$, $r \in \mathcal{R} = \{P1, P2, P3, P4, W, M1, M2\}$, and $c \in \mathcal{C} = \{POX, WGS, MeOH\}$. Here, N_2 is not included in the chemical component set $\mathcal{K}$, as air is not a raw material. Product Gas-1 represents the outlet of the CO_2 separator and $Crude$ represents the crude liquid methanol that leaves the VLE-3. The separation phenomena $VLPC$ and GP stand for vapor-liquid phase contact and gas permeation, respectively. In the separation material set $\mathcal{M}$, VLI stands for vapor-liquid interface and CM denotes the CO_2 membrane. The 50×4 superstructure for the base design has the following sets: $k \in \mathcal{K} = \{CH_4, O_2, H_2, CO, CO_2, H_2O, CH_3OH\}$, $f \in \mathcal{F} = \{Crude\}$, $p \in \mathcal{P} = \{Product, Water, Purge\}$, $s \in \mathcal{S} = \{VLPC\}$, $m \in \mathcal{M} = \{VLI\}$, $r \in \mathcal{R} = null$, and $c \in \mathcal{C} = null$. As no reactions are allowed, the sets of reactions, $\mathcal{R}$ and catalysts, $\mathcal{C}$ are empty. Additionally, as membrane-based separations are not present, separation phenomena set, $\mathcal{S}$, only includes $VLPC$ and separation material set, $\mathcal{M}$ only contains VLI. The 7×20 superstructure for intensified process synthesis, on the other hand, has the following sets:

$k \in \mathcal{K} = \{CH_4, O_2, N_2, H_2, CO, CO_2, H_2O, CH_3OH\}$, $f \in \mathcal{F} = \{NG, Oxy, Steam, Air\}$, $p \in \mathcal{P} = \{Crude\text{-}1, Crude\text{-}2, Gas\text{-}1, Gas\text{-}2, Liquid, Purge\}$, $s \in \mathcal{S} = \{VLPC, GP\}$, $m \in \mathcal{M} = \{VLI, CM, PM, MM\}$, $r \in \mathcal{R} = \{P1, P2, P3, P4, W, M1, M2\}$, and $c \in \mathcal{C} = \{POX, WGS, MeOH\}$. Here, the products $Crude$-1, $Crude$-2, and Gas-2 denotes the main product of the MeOH reactor (from block $B_{5,20}$), permeate side product (from block $B_{1,8}$), and air outlet from the POX reactor (from block $B_{2,14}$), respectively. Additionally, enabling materiel PM and MM stands for the POX membrane and the MeOH membrane. The following sets are included in the 50×4 superstructure: $k \in \mathcal{K} = \{CH_4, O_2, H_2, CO, CO_2, H_2O, CH_3OH\}$, $f \in \mathcal{F} = \{Crude\text{-}1, Crude\text{-}2\}$, $p \in \mathcal{P} = \{Product, Water, Purge\}$, $s \in \mathcal{S} = \{VLPC\}$, $m \in \mathcal{M} = \{VLI\}$, $r \in \mathcal{R} = null$, and $c \in \mathcal{C} = null$. The minimum purity requirement of methanol in the final product is 99.5% (vol./vol.) ($y_{k=CH_3OH,p=Product}^{min,prod} \geq 0.995$).

Results and Discussion

Base Case Optimization

As a first step to establish the base case, we perform a technoeconomic evaluation of the conventional design presented in Figure 2. We perform process simulation while allowing the temperatures of the reactors to vary within allowable temperature ranges. Additionally, we pre-specify the operating temperatures (apart from the reactors) and pressures as well as the binary variables denoting the positions of all fixed phenomena and equipment. This reduces the building block-base model to a non-linear program (NLP). The 5×14 block-based model has 1891 variables, 2576 equations, and 5617 nonlinear terms, when the distillation column is optimized separately. We use a 50×4 model with 3245 variables, 6306 equations, and 15100 nonlinear terms to represent the distillation column alone. We solved the models in GAMS 28.2 environment using ANTIGONE v28.2.0.[66] The estimated TAP of the conventional process is 11.8 MM$/yr. The annual methanol production rate is 164750 ton/yr, which is equivalent to an annual income of 65.9 MM$/yr. The annualized operating cost (AOC) and the fixed capital investment (FCI) are found to be 40.6 MM$/yr and 80.5 MM$/yr, respectively. Additionally, the annual return on investment (ROI) is 18.2%/yr. and the annual CO_2-equivalent emission is 155.3 kt CO_2/yr. (see Table 2 for details).

[**Figure 6 about here**]

While optimizing the conventional design, we allow the block temperatures and the pressures except the reactor pressure to vary. We fix the reactor pressure to be the same as

the base design. The 5×14 model is solved in 3544 CPU seconds in ANTIGONE v28.2.0. The distillation column model (50×4 superstructure) is solved with tray numbers varying between 15 to 50. The model with 46 trays in the distillation column is solved in 374 CPU seconds. The overall process after optimization (Figure 6) can yield a total annual profit (TAP) of 22.9 MM\$/yr. There are two main reasons behind this increase in the TAP. Firstly, the methanol yield has increased by 4%, because of reduced purging and increased recycle. Secondly, the compression work has deceased significantly, which decreases the compressor capital cost and the electricity cost by by 57% and 71%, respectively. As VLE-3 operates at the same pressure as the MeOH reactor, no additional compressor is needed in the recycle loop. Additionally, as the block pressures are allowed to vary, instead of a single compressor, multiple compressors with inter-coolers are selected. This reduces the energy consumption of the compressor operation. The ROI is increased by 80% and the annual emission is also reduced to 89 kt CO_2/yr.

[**Table 2 about here**]

Intensified Process Synthesis

The optimization of the conventional design shows that it is possible to improve the process profitability and sustainability. Thus, a 7×20 superstructure is used which considers all possibilities of process integration and intensification. As the 7×20 model is significantly large, to obtain a good initial solution, the model is warm started with solution obtained from the base case optimization. Once the initial solution is obtained, we step-by-step free the ranges of variables to allow more alternatives and activate design constraints. In the final optimization run, all the variable bounds and design constraints are enforced. To ensure realistic design, we impose several additional constraints. For instance, the inlet CO_2 composition in MeOH reactor is now allowed to vary between 3–10% to ensure the Cu-ZnO-Al_2O_3 catalyst activity.[67] Although the ideal syngas ratio is close to 2-2.05 for methanol synthesis,[68] the actual molar ratio is dictated by the stoichiometric number, SN = (H_2 - CO_2)/(CO + CO_2),[69] which considers the presence of CO_2 in the syngas as it also consumes H_2 by the RWGS reaction (Eq. M3). Therefore, to ensure the presence of excess H_2 for converting all CO and CO_2 in the MeOH reactor, we impose $H_2 \geq 2 \times$CO + 3×CO_2 at the MeOH reactor inlet. The 7×20 superstructure model consists of 4467 continuous variables, 58 binary variables, 6501 equations, and 14232 nonlinear terms. We solve the model using ANTIGONE v28.2.0 in 10,074 CPU seconds and the 50×4 model of the distillation column in 2014 CPU seconds. The TAP of the intensified process is 34.4 MM\$/yr and the obtained process flowsheet is presented in Figure 7. A detailed comparison

of the costs between the three design variants, namely the conventional design (Figure 2), optimized design (Figure 6) and the novel intensified design (Figure 7), is provided in Table 2. Here, the hot utility cost includes the cost of all associated heating requirement such as steam super-heating, the nature gas and pure oxygen preheating, the syngas preheating before the WGS reactor, the liquid preheating before the methanol distillation column, and the re-boiler duty. Similarly, cold utility cost includes precooling before VLE separators, compressor intercooling, and condenser duty. On the same note, electricity cost includes the cost of operating the compressors in all three designs.

[**Figure 7 about here**]

The intensified flowsheet (Figure 7) has some major differences compared to the conventional design (Figure 2). The WGS reactor and the CO_2 membrane separator are excluded from the flowsheet. Furthermore, both the conventional POX and MeOH reactors are now replaced by intensified membrane reactors which are denoted by POX_MR and MeOH_MR, respectively. The POX_MR uses steam as feed and the generated syngas has a H_2 to CO ratio close to 2.0. Moreover, this ratio is around 4.0 at the MeOH_MR inlet because of the recycle flow. As the molar composition of CO_2 at the MeOH_MR inlet satisfies the minimum allowable value of 3%, the CO_2 membrane separator is not needed anymore. The POX_MR operates at a higher pressure (39 bar) compared to the conventional POX reactor. In case of POX reaction, the number of moles at the inlet almost doubles that of the outlet. Therefore, it is beneficial to compress the raw materials before feeding it to the reactor. Additionally, as the methanol synthesis reaction takes place at a higher pressure, the syngas feed to this reactor has to be compressed to a higher pressure. To reduce the energy consumption for compression, the raw materials are compressed and the POX_MR is also operated at a higher pressure than the conventional case. Along with natural gas, steam enters the reaction side of the POX_MR, whereas air enters the shell side of the reactor. Due to the partial pressure difference across the membrane, oxygen separation from the feed air occurs simultaneously. The separated oxygen enters the reaction zone and is subsequently consumed. Because of the exothermic nature of the partial oxidation reaction, the reactor temperature increases and reaches the maximum allowable membrane temperature of 1173 K after the gases reach about 80% of the length of the reactor tubes. However, at this condition the CH_4 conversion is only 33%. To increase the conversion and allow the reaction temperature to rise further, the final 20% of the reactor tube is considered to be made of metal tubes, instead of using membranes. To provide the required oxygen for POX reactions, pure oxygen enters the reaction zone as a side feed at the 80% length of the reactor. These type of partially intensified design with side feed reactor is not uncommon and

has been previously reported in the literature.[48] The produced syngas leaves the POX_MR at 1573 K and exchanges heat with natural gas, air, and oxygen. These reduces the syngas temperature to 716 K. A cooler is used to further reduce the operating temperature of the VLE-1 separator. The syngas from VLE-1 is compressed to 52 bar before it enters to the MeOH_MR. Compared to the conventional MeOH reactor, the intensified MeOH_MR operates at a lower pressure. Because of the *in situ* removal of the product methanol and water, the membrane reactor can produce the same amount of methanol at a lower pressure.[48] The permeate side of the MeOH_MR operates at 1 bar with air as the sweep gas. The outlet of the permeate side enters VLE-3 separator for methanol and water separation. The crude methanol product from VLE-3 has a methanol purity of 93% (vol./vol.). The main MeOH_MR product enters the VLE-2 separator, and the crude methanol leaves this separator as liquid with 95% (vol./vol.) purity. Crude methanol from both the VLE-2 and VLE-3 separators enters the VLE-4 separator to release the dissolved gases at 1 bar. Lastly, the crude methanol enters the distillation column with 30 stages. The crude methanol enters to the distillation column at three different trays (trays no. 19, 21, and 22).

Technoeconomic Analysis (TEA)

The annual income of the conventional design, the optimized design, and the novel intensified design are 65.9 MM$/yr., 68.6 MM$/yr., and 75.6 MM$/yr., respectively. Compared to the conventional design, the intensified process has 15% higher annual income. This is mainly due to the higher recycle ratio and the *in situ* separation of products in the MeOH_MR reactor. The intensified process also has lower TAC compared to both designs. The TAC components are presented in Figure 8a–c. In the conventional design, the annual raw material cost is 54.7% of the TAC. These costs are 64.2% and 61.5%, for the optimal base design and the intensified design, respectively. The actual raw martial cost remains unchanged in the optimized design, but it has higher percent contribution in TAC compared to the conventional design. The raw material consumption cost for the intensified process is 25.4 MM$/yr, which is 14% less compared to the conventional design. The raw material cost is reduced mainly due to the reduction of pure oxygen consumption within the POX_MR reactor. As the POX_MR reactor separates the required oxygen from the air and consumes it *in situ*, the membrane reactor consumes less amount of expensive pure oxygen. However, the overall steam consumption of the intensified process is higher compared to the other processes. The higher steam consumption at POX_MR improves the syngas quality, which in turn help exclude the WGS reactor from the flowsheet. The intensified process also consumes less utilities. The utility cost represents only 12.9% of the TAC. The combined

cost of the hot and cold utilities is reduced by 39% from the conventional design due to heat integration. Electricity is mainly consumed to operate the syngas compressor. As the intensified MeOH_MR operates at a lower pressure (52 bar) compared to the conventional MeOH reactors (75 bar), the intensified process consumes less electricity compared to the conventional process. In fact, the annual electricity consumption cost of the intensified design is one-third of that of the conventional design.

[**Figure 8 about here**]

The FCI of the three design cases are shown in Figure 8d. The total FCI is segregated among the reforming, compression, methanol synthesis, and separation sections of the process. The POX_MR of the intensified process is more expensive due to the cost of the membrane tubes. The intensified process also requires expensive methanol synthesis equipment compared to the other designs. However, the intensified design does not have the WGS reactor and the CO_2 membrane separator, which help reduce the overall costs compared to other designs. The total FCI of the intensified process is 21% lower and 8% higher compared to the conventional and optimized design, respectively. Even though the intensified process requires expensive equipment compared to the optimized process, it has higher TAP because of higher methanol production. The methanol production costs are $328/tonne, $266/tonne, and $218/tonne for the conventional process, the optimized process, and the intensified process, respectively. Additionally, the intensified process has higher ROI. The ROI of the conventional design and the optimized design are 18.2%/yr. and 32.8%/yr., respectively. On the other hand, the intensified process has an annual ROI of 42.0%/yr., which makes the process more profitable than others.

Environmental Impact Assessment

Compared to the conventional designs, the intensified design is both economically more profitable and environmentally more sustainable (Figure 9). Because of the low compression work requirement, the indirect CO_2-equivalent emission due to electricity consumption is less for the intensified design. Similarly, due to heat integration, the CO_2-equivalent emission for burning fuel is reduced to half. The CO_2-equivalent emission for processing shale gas to supply the feed methane is equal for all three designs. However, as the intensified process consumes less pure oxygen, it has less indirect CO_2-equivalent emission for oxygen separation. Finally, as the MeOH_MR has higher methanol yield, it converts most of the CO_2 to methanol. Thus, the intensified process emits less direct CO_2 to the environment compared to the other two processes.

[**Figure 9 about here**]

Conclusions

The shale gas boom has increased the production of natural gas in the U.S. However, the sparse locations of many shale gas wells hinder the use of this abundant natural resource. We synthesized a novel intensified process flowsheet for methanol synthesis from natural gas at a scale amenable to shale gas utilization at the source. The obtained flowsheet has modular structure that can be easily transported to remote locations. For the process synthesis, we used building block-based representation. The reactors were modeled with detailed reaction kinetics. To avoid the complexity associated with thermodynamic models, we used data driven surrogate models to estimate the thermodynamic properties. The new intensified process requires fewer major equipment, has higher total annual profit and higher return on investment and, at the same time, has lower GHG emission. Due to heat integration, the process also consumes less hot and cold utilities. The intensified partial oxidation reactor reduces the consumption of expensive pure oxygen by 34%. Similarly, the intensified methanol synthesis reactor improves the overall methanol yield via *in situ* product removal. This improves the overall methanol purity and reduces the burden of further purification using distillation. All of these increase the annual return on investment. Additionally, the process is more environmentally sustainable as it has significantly less GHG emission. One thing is worth mentioning here is that, to access the actual benefit of the presented novel flowsheet, detailed simulation needs to be performed. However, this preliminary process synthesis gives us an indication that, to make the methanol production process more profitable and sustainable, process intensification has to be considered during the synthesis stage of the process.

Acknowledgement

Data Availability Statement

The data that support the findings of this study are available from the corresponding author upon reasonable request.

Supporting Information

Additional supporting information may be found online in the Supporting Information.

References

[1] Arthur JD, Bohm BK, Cornue D, et al. Environmental considerations of modern shale gas development. In: *SPE annual technical conference and exhibition.* Society of Petroleum Engineers. 2009; .

[2] Joskow PL. Natural gas: from shortages to abundance in the United States. *American Economic Review.* 2013; 103(3):338–43.

[3] Wang Q, Chen X, Jha AN, Rogers H. Natural gas from shale formation–the evolution, evidences and challenges of shale gas revolution in United States. *Renewable and Sustainable Energy Reviews.* 2014;30:1–28.

[4] US Energy Information Administration, Annual Energy Outlook 2019. https://www.eia.gov/outlooks/archive/aeo19/pdf/AEO2019.pdf (accessed June 2021).

[5] US Energy Information Administration, Annual Energy Outlook 2015. https://www.eia.gov/outlooks/archive/aeo15/pdf/0383(2015).pdf (accessed June 2021).

[6] Petak K, Chikkatur A, Manik J, Palagummi S, Greene K. North American Midstream Infrastructure Through 2035: Leaning into the Headwinds. *The INGAA Foundation, Inc.* 2016;20.

[7] US Energy Information Administration, Natural Gas Vented and Flared. https://www.eia.gov/dnav/ng/hist/n9040us2a.htm (accessed June 2021).

[8] Yang M. Modular fuels/chemical production from shale gas. In: *Towards Sustainable Chemical Processes.* Elsevier. 2020; pp. 379–398.

[9] Olah GA. Beyond oil and gas: the methanol economy. *Angewandte Chemie International Edition.* 2005;44(18):2636–2639.

[10] Santos BA, Loureiro JM, Ribeiro AM, Rodrigues AE, Cunha AF. Methanol production by bi-reforming. *The Canadian Journal of Chemical Engineering.* 2015;93(3):510–526.

[11] Alvarado M. Methanol Industry Overview. *Opportunities and Challenges for Methanol as a Global Liquid Energy Carrier.* 2017;.

[12] Methanol Institute: Methanol Price and Supply/Demand. https://www.methanol.org/methanol-price-supply-demand (accessed June 2021).

[13] Nestler F, Krüger M, Full J, Hadrich MJ, White RJ, Schaadt A. Methanol synthesis–industrial challenges within a changing raw material landscape. *Chemie Ingenieur Technik.* 2018;90(10):1409–1418.

[14] Luo S, Zeng L, Xu D, Kathe M, Chung E, Deshpande N, Qin L, Majumder A, Hsieh TL, Tong A, et al. Shale gas-to-syngas chemical looping process for stable shale gas conversion to high purity syngas with a H 2: CO ratio of 2: 1. *Energy & Environmental Science.* 2014;7(12):4104–4117.

[15] Noureldin MM, Elbashir NO, El-Halwagi MM. Optimization and selection of reforming approaches for syngas generation from natural/shale gas. *Industrial & Engineering Chemistry Research.* 2014;53(5):1841–1855.

[16] Dybkjær I, Aasberg-Petersen K. Synthesis gas technology large-scale applications. *The Canadian Journal of Chemical Engineering.* 2016;94(4):607–612.

[17] Al-Sayari SA. Recent developments in the partial oxidation of methane to syngas. *The Open Catalysis Journal.* 2013;6(1).

[18] Wittich K, Krämer M, Bottke N, Schunk SA. Catalytic dry reforming of methane: Insights from model systems. *ChemCatChem.* 2020;12(8):2130–2147.

[19] Blumberg T, Morosuk T, Tsatsaronis G. A comparative exergoeconomic evaluation of the synthesis routes for methanol production from natural gas. *Applied Sciences.* 2017;7(12):1213.

[20] Blumberg T, Tsatsaronis G, Morosuk T. On the economics of methanol production from natural gas. *Fuel.* 2019;256:115824.

[21] Medrano-García J, Ruiz-Femenia R, Caballero J. Multi-objective optimization of combined synthesis gas reforming technologies. *Journal of CO2 Utilization*. 2017;22:355–373.

[22] Martinez-Gomez J, Nápoles-Rivera F, Ponce-Ortega JM, El-Halwagi MM. Optimization of the production of syngas from shale gas with economic and safety considerations. *Applied Thermal Engineering*. 2017;110:678–685.

[23] Julian-Duran LM, Ortiz-Espinoza AP, El-Halwagi MM, Jimenez-Gutierrez A. Techno-economic assessment and environmental impact of shale gas alternatives to methanol. *ACS Sustainable Chemistry & Engineering*. 2014; 2(10):2338–2344.

[24] Ehlinger VM, Gabriel KJ, Noureldin MM, El-Halwagi MM. Process design and integration of shale gas to methanol. *ACS Sustainable Chemistry & Engineering*. 2014;2(1):30–37.

[25] Gao J, You F. Can modular manufacturing be the next game-changer in shale gas supply chain design and operations for economic and environmental sustainability? *ACS Sustainable Chemistry & Engineering*. 2017;5(11):10046–10071.

[26] Yang M, You F. Modular methanol manufacturing from shale gas: Techno-economic and environmental analyses of conventional large-scale production versus small-scale distributed, modular processing. *AIChE Journal*. 2018; 64(2):495–510.

[27] Carrasco JC, Lima FV. An optimization-based operability framework for process design and intensification of modular natural gas utilization systems. *Computers & Chemical Engineering*. 2017;105:246–258.

[28] Kruglov AV. Methanol synthesis in a simulated countercurrent moving-bed adsorptive catalytic reactor. *Chemical engineering science*. 1994;49(24):4699–4716.

[29] da Silva MJ. Synthesis of methanol from methane: Challenges and advances on the multi-step (syngas) and one-step routes (DMTM). *Fuel Processing Technology*. 2016;145:42–61.

[30] Farsi M, Jahanmiri A. Methanol production in an optimized dual-membrane fixed-bed reactor. *Chemical Engineering and Processing: Process Intensification*. 2011;50(11-12):1177–1185.

[31] Maréchal F, Heyen G, Kalitventzeff B. Energy savings in methanol synthesis: use of heat integration techniques and simulation tools. *Computers & chemical engineering*. 1997;21:S511–S516.

[32] Morar M, Agachi PS. Important contributions in development and improvement of the heat integration techniques. *Computers & Chemical Engineering*. 2010;34(8):1171–1179.

[33] Tian Y, Demirel SE, Hasan MMF, Pistikopoulos EN. An overview of process systems engineering approaches for process intensification: State of the art. *Chemical Engineering and Processing-Process Intensification*. 2018;133:160–210.

[34] Khanipour M, Mirvakili A, Bakhtyari A, Farniaei M, Rahimpour MR. Enhancement of synthesis gas and methanol production by flare gas recovery utilizing a membrane based separation process. *Fuel Processing Technology*. 2017; 166:186–201.

[35] Keshavarz A, Mirvakili A, Chahibakhsh S, Shariati A, Rahimpour M. Simultaneous methanol production and separation in the methanol synthesis reactor to increase methanol production. *Chemical Engineering and Processing-Process Intensification*. 2020;158:108176.

[36] Arora A, Iyer SS, Bajaj I, Hasan MF. Optimal methanol production via sorption-enhanced reaction process. *Industrial & Engineering Chemistry Research*. 2018;57(42):14143–14161.

[37] Demirel SE, Li J, Hasan MMF. Systematic process intensification using building blocks. *Computers & Chemical Engineering*. 2017;105:2–38.

[38] Zhu T, Flytzani-Stephanopoulos M. Catalytic partial oxidation of methane to synthesis gas over Ni–CeO2. *applied catalysis A: General*. 2001;208(1-2):403–417.

[39] De Groote AM, Froment GF. Simulation of the catalytic partial oxidation of methane to synthesis gas. *Applied Catalysis A: General*. 1996;138(2):245–264.

[40] De Smet C, De Croon M, Berger R, Marin G, Schouten J. Design of adiabatic fixed-bed reactors for the partial oxidation of methane to synthesis gas. Application to production of methanol and hydrogen-for-fuel-cells. *Chemical Engineering Science*. 2001;56(16):4849–4861.

[41] Amadeo N, Laborde M. Hydrogen production from the low-temperature water-gas shift reaction: kinetics and simulation of the industrial reactor. *International journal of hydrogen energy*. 1995;20(12):949–956.

[42] Graaf G, Stamhuis E, Beenackers A. Kinetics of low-pressure methanol synthesis. *Chemical Engineering Science*. 1988; 43(12):3185–3195.

[43] Slotboom Y, Bos M, Pieper J, Vrieswijk V, Likozar B, Kersten S, Brilman D. Critical assessment of steady-state kinetic models for the synthesis of methanol over an industrial Cu/ZnO/Al2O3 catalyst. *Chemical Engineering Journal*. 2020; 389:124181.

[44] Lacerda de Oliveira Campos B, Herrera Delgado K, Pitter S, Sauer J. Development of Consistent Kinetic Models Derived from a Microkinetic Model of the Methanol Synthesis. *Industrial & Engineering Chemistry Research*. 2021; 60(42):15074–15086.

[45] Bisotti F, Fedeli M, Prifti K, Galeazzi A, Dell'Angelo A, Barbieri M, Pirola C, Bozzano G, Manenti F. Century of Technology Trends in Methanol Synthesis: Any Need for Kinetics Refitting? *Industrial & Engineering Chemistry Research*. 2021;60(44):16032–16053.

[46] Bussche KV, Froment G. A steady-state kinetic model for methanol synthesis and the water gas shift reaction on a commercial $Cu/ZnO/Al_2O_3$ catalyst. *Journal of Catalysis*. 1996;161(1):1–10.

[47] Chen L, Jiang Q, Song Z, Posarac D. Optimization of methanol yield from a Lurgi reactor. *Chemical engineering & technology*. 2011;34(5):817–822.

[48] Monjur MS, Demirel SE, Li J, Hasan MMF. SPICE_MARS: A Process Synthesis Framework for Membrane-Assisted Reactive Separations. *Industrial & Engineering Chemistry Research*. 2021;60(20):7635–7655.

[49] Demirel SE, Li J, Hasan MMF. A general framework for process synthesis, integration, and intensification. *Industrial & Engineering Chemistry Research*. 2019;58(15):5950–5967.

[50] Li J, Demirel SE, Hasan MMF. Process synthesis using block superstructure with automated flowsheet generation and optimization. *AIChE Journal*. 2018;64(8):3082–3100.

[51] Li J, Demirel SE, Hasan M. Fuel gas network synthesis using block superstructure. *Processes*. 2018;6(3):23.

[52] Li J, Demirel SE, Hasan M. Building block-based synthesis and intensification of work-heat exchanger networks (WHENS). *Processes*. 2019;7(1):23.

[53] Demirel SE, Li J, El-Halwagi M, Hasan MMF. Sustainable Process Intensification Using Building Blocks. *ACS Sustainable Chemistry & Engineering*. 2020;8(48):17664–17679.

[54] Demirel SE, Li J, Hasan MMF. Membrane Separation Process Design and Intensification. *Industrial & Engineering Chemistry Research*. 2021;60(19):7197–7217.

[55] Monjur MS, Demirel SE, Li J, Hasan MMF. A Computer-Aided Platform for Simultaneous Process Synthesis and Intensification. In: *Computer Aided Chemical Engineering*, vol. 50. Elsevier. 2021; pp. 287–293.

[56] Alsuhaibani AS, Afzal S, Challiwala M, Elbashir NO, El-Halwagi MM. The impact of the development of catalyst and reaction system of the methanol synthesis stage on the overall profitability of the entire plant: A techno-economic study. *Catalysis Today*. 2020;343(1):191–198.

[57] Kim S, Ryi SK, Lim H. Techno-economic analysis (TEA) for CO2 reforming of methane in a membrane reactor for simultaneous CO2 utilization and ultra-pure H2 production. *International Journal of Hydrogen Energy*. 2018; 43(11):5881–5893.

[58] Luo H, Wei Y, Jiang H, Yuan W, Lv Y, Caro J, Wang H. Performance of a ceramic membrane reactor with high oxygen flux Ta-containing perovskite for the partial oxidation of methane to syngas. *Journal of Membrane Science*. 2010; 350(1-2):154–160.

[59] Luo S, Stevens KA, Park JS, Moon JD, Liu Q, Freeman BD, Guo R. Highly CO2-selective gas separation membranes based on segmented copolymers of poly (ethylene oxide) reinforced with pentiptycene-containing polyimide hard segments. *ACS applied materials & interfaces*. 2016;8(3):2306–2317.

[60] Struis RPWJ, Stucki S, Wiedorn M. A membrane reactor for methanol synthesis. *Journal of membrane science*. 1996; 113(1):93–100.

[61] Luyben WL. Design and control of a methanol reactor/column process. *Industrial & engineering chemistry research*. 2010;49(13):6150–6163.

[62] Yao L, Li M, Hu Y, Wang Q, Liu X. Comparative study of upgraded CO2 transcritical air source heat pump systems with different heat sinks. *Applied Thermal Engineering*. 2021;184:116289.

[63] Luo H, Bildea CS, Kiss AA. Novel heat-pump-assisted extractive distillation for bioethanol purification. *Industrial & Engineering Chemistry Research*. 2015;54(7):2208–2213.

[64] Chen Q, Dunn JB, Allen DT. Greenhouse Gas Emissions of Transportation Fuels from Shale Gas-Derived Natural Gas Liquids. *Procedia CIRP*. 2019;80:346–351.

[65] Darde A, Prabhakar R, Tranier JP, Perrin N. Air separation and flue gas compression and purification units for oxy-coal combustion systems. *Energy Procedia*. 2009;1(1):527–534.

[66] Misener R, Floudas CA. ANTIGONE: algorithms for continuous/integer global optimization of nonlinear equations. *Journal of Global Optimization*. 2014;59(2-3):503–526.

[67] Klier K, Chatikavanij V, Herman R, Simmons G. Catalytic synthesis of methanol from COH2: IV. The effects of carbon dioxide. *Journal of Catalysis*. 1982;74(2):343–360.

[68] Løvik I, Rønnekleiv M, Olsvik O, Hertzberg T. Estimation of a deactivation model for the methanol synthesis catalyst from historic process data. In: *Computer Aided Chemical Engineering*, vol. 9. Elsevier. 2001; pp. 219–224.

[69] Lange JP. Methanol synthesis: a short review of technology improvements. *Catalysis Today*. 2001;64(1-2):3–8.

[70] Demirhan CD, Tso WW, Powell JB, Pistikopoulos EN. Sustainable ammonia production through process synthesis and global optimization. *AIChE Journal*. 2019;65(7):e16498.

[71] Atsonios K, Panopoulos KD, Kakaras E. Investigation of technical and economic aspects for methanol production through CO2 hydrogenation. *International Journal of hydrogen energy*. 2016;41(4):2202–2214.

[72] Ho MT, Allinson GW, Wiley DE. Reducing the cost of CO2 capture from flue gases using membrane technology. *Industrial & Engineering Chemistry Research*. 2008;47(5):1562–1568.

[73] Woods DR. *Rules of thumb in engineering practice*. John Wiley & Sons. 2007.

[74] Struis R, Stucki S. Verification of the membrane reactor concept for the methanol synthesis. *Applied Catalysis A: General*. 2001;216(1-2):117–129.
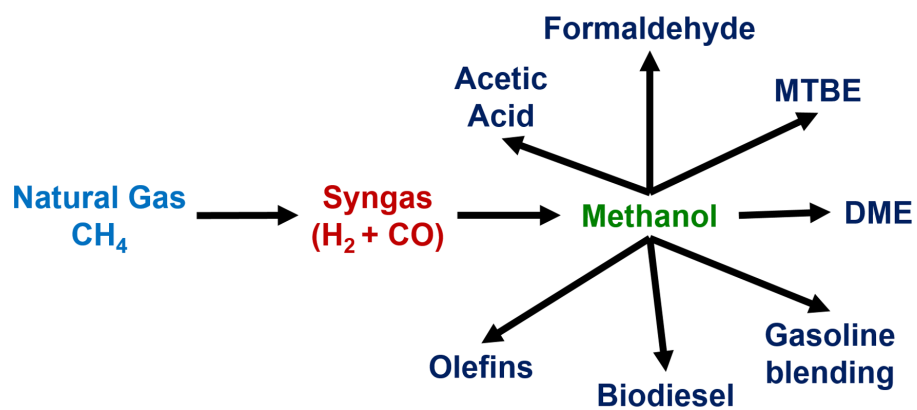
List of Figures

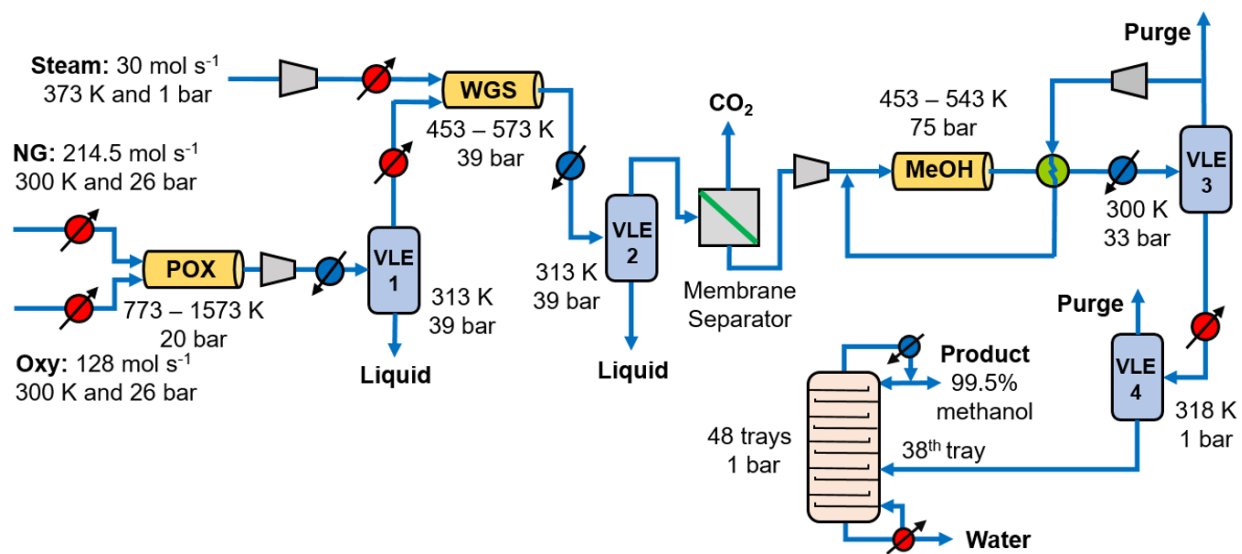**Figure 1:** Natural gas conversion to chemicals and fuels via methanol.

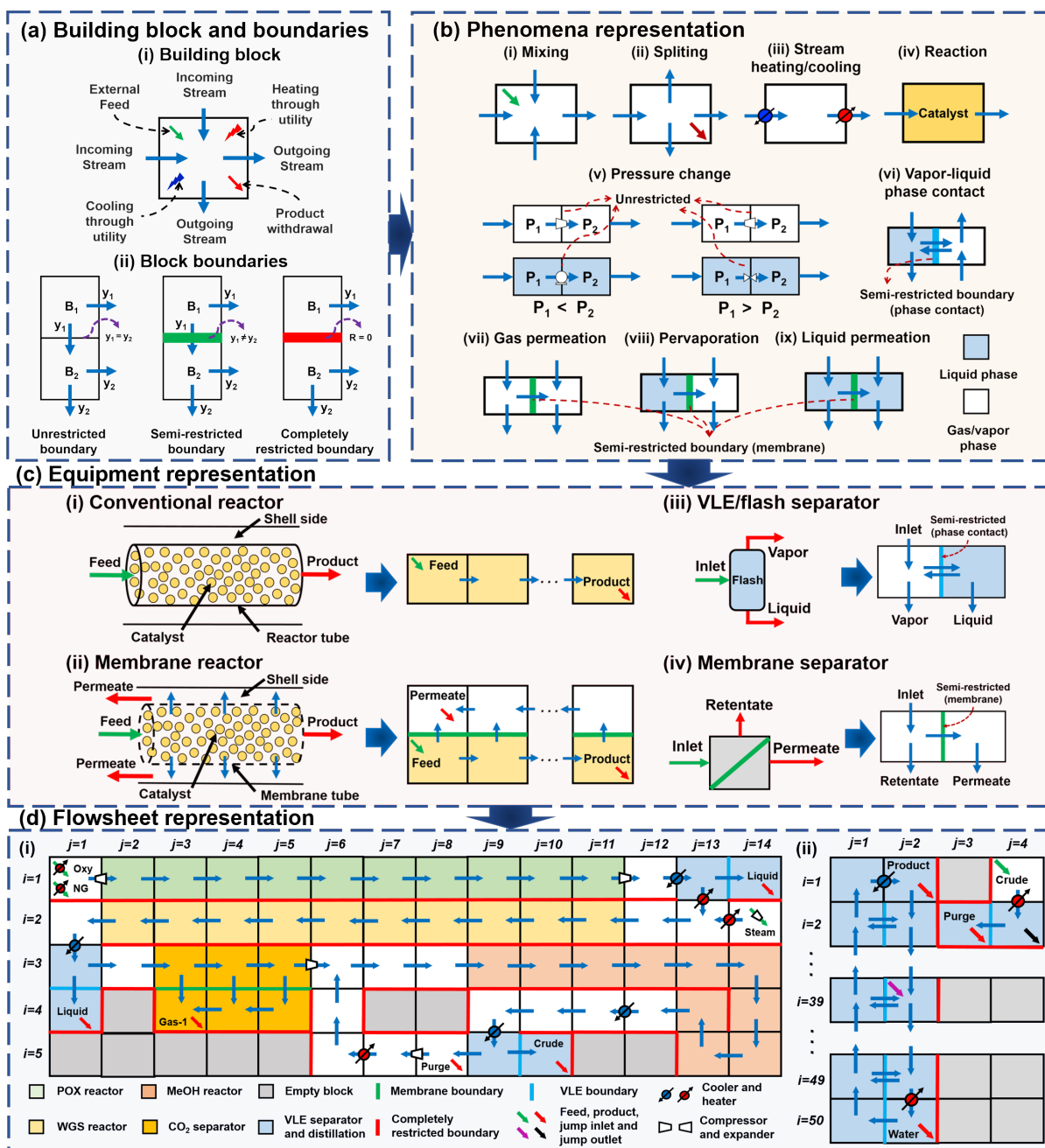**Figure 2:** Conventional methanol process flowsheet.

Figure 3: Building block-based representation of chemical processes. (a) Each building block allows material & energy flows through any of the four boundaries. Neighbouring blocks can have one of the three types of common block boundaries. (b) Many fundamental physicochemical phenomena can be represented by using different numbers of blocks. (c) By arranging several phenomena representing blocks, different types of unit operations are obtained. (d) A collection of building blocks depicted here represents the conventional methanol process.
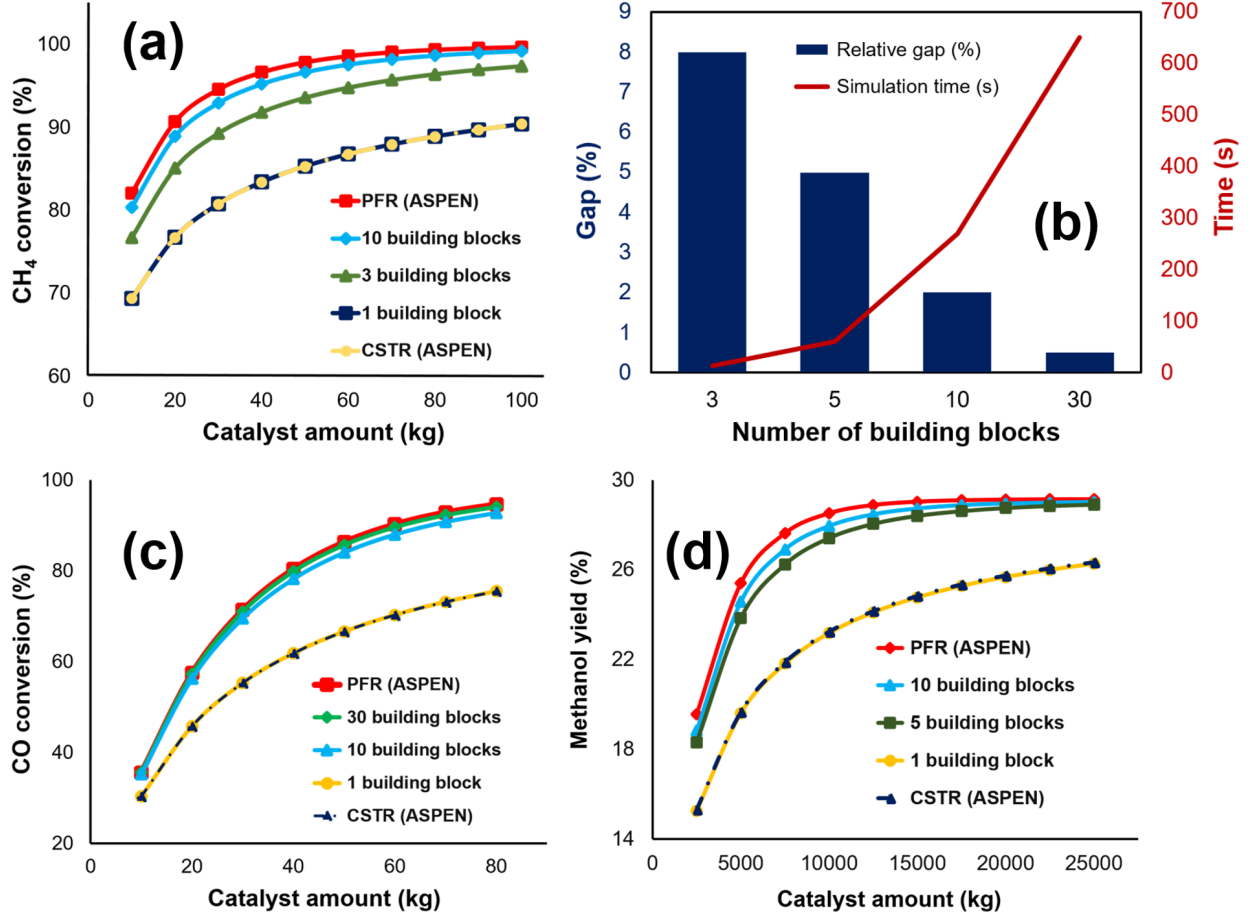
Figure 4: Accuracy and computational efficacy of building block-based reactor modeling: (a) CH_4 conversion results obtained from Aspen Plus and building block representation in POX reactor; (b) relative gaps between the Aspen Plus and the building block-based simulation results and simulation times needed by the building block model for n-block-CSTR; (c) CO conversion in WGS reactor; and (d) methanol yield in MeOH reactor.
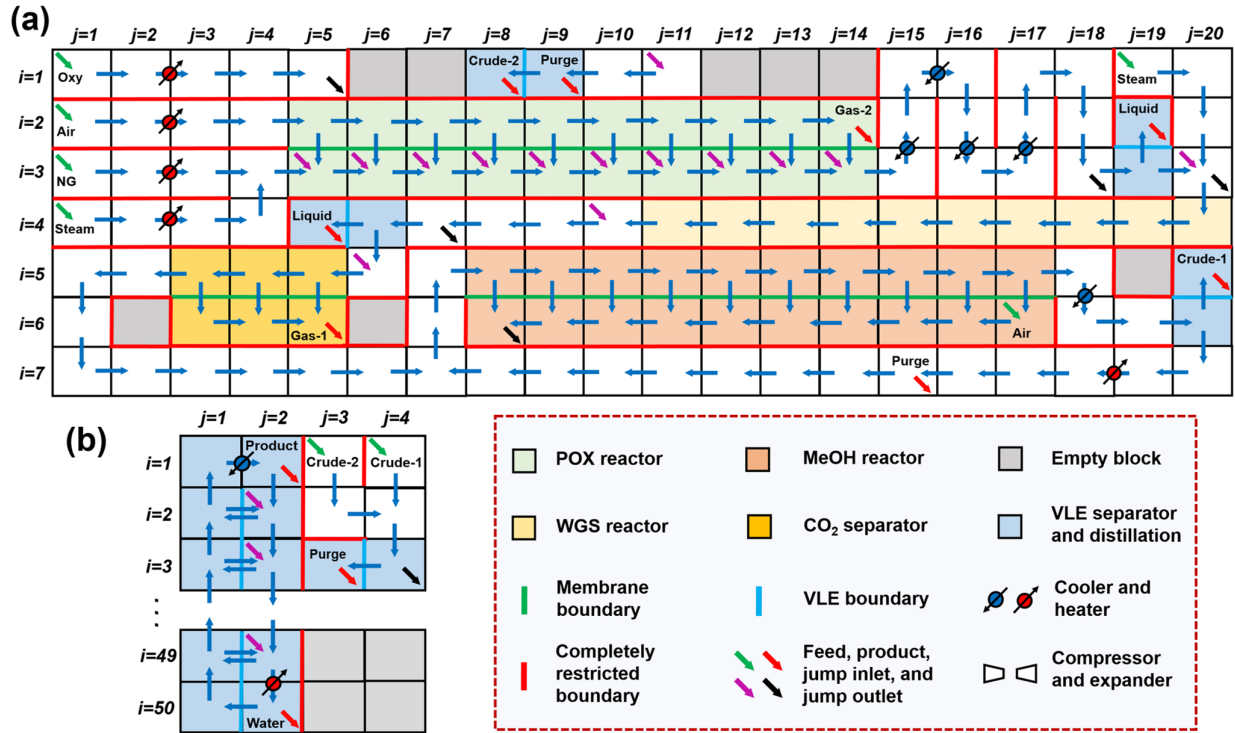
Figure 5: Building block superstructure considered for intensified methanol process synthesis.
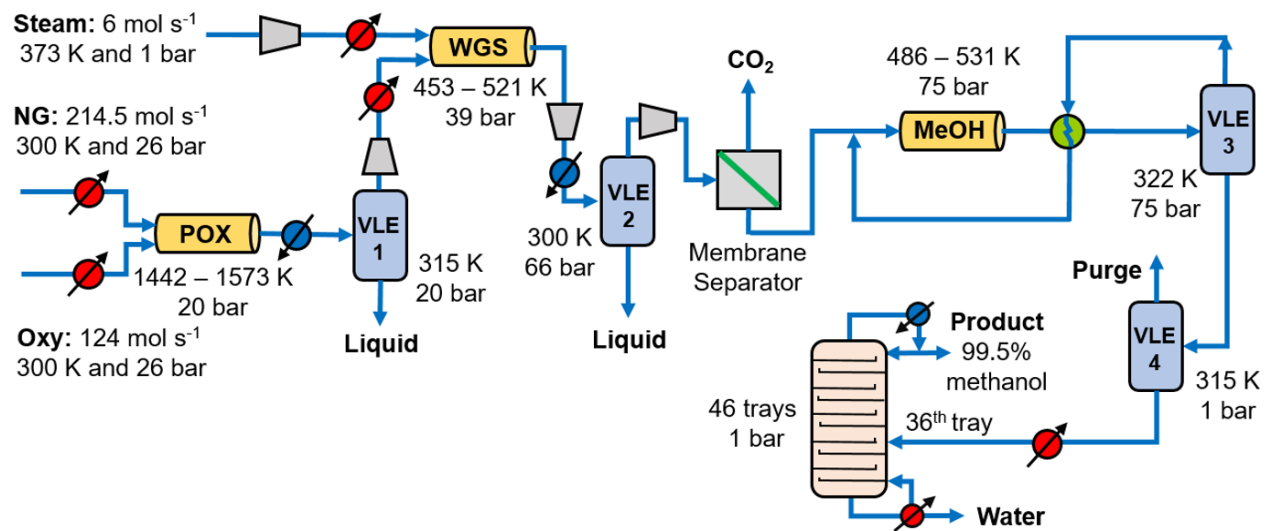
Figure 6: An optimized but non-intensified, conventional methanol synthesis process flowsheet.
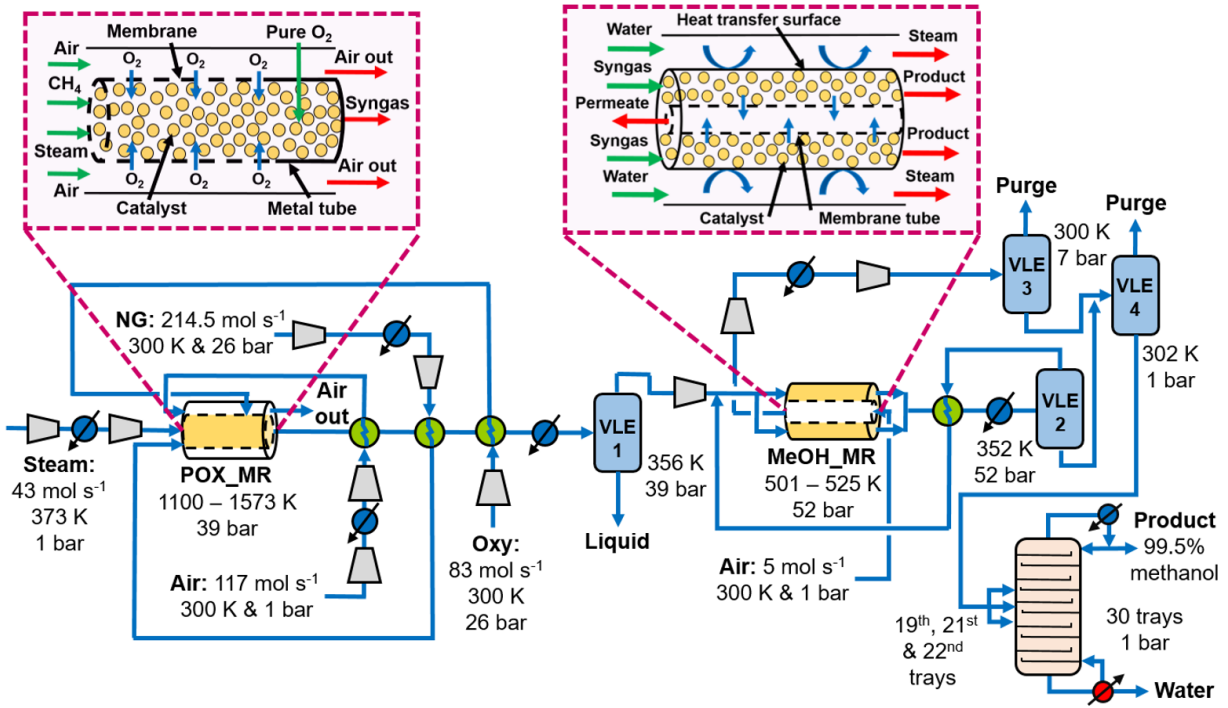
Figure 7: Novel intensified and heat integrated methanol synthesis process flowsheet.
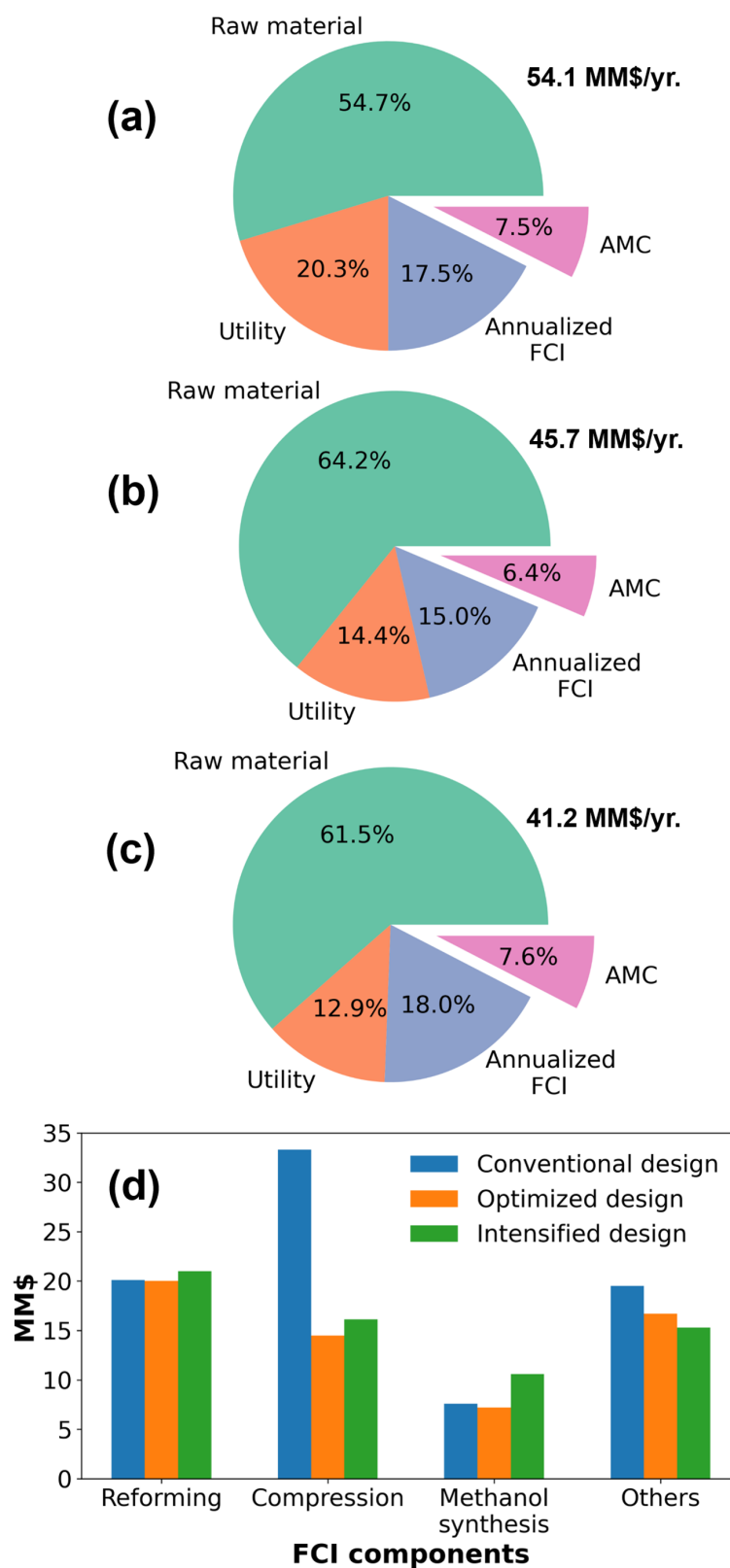
Figure 8: Percent contribution of TAC components: (a) conventional design, (b) optimized design, and (c) novel intensified design. The values beside each pie-chart represent the total annual costs. The breakdown of the FCI is shown in (d).
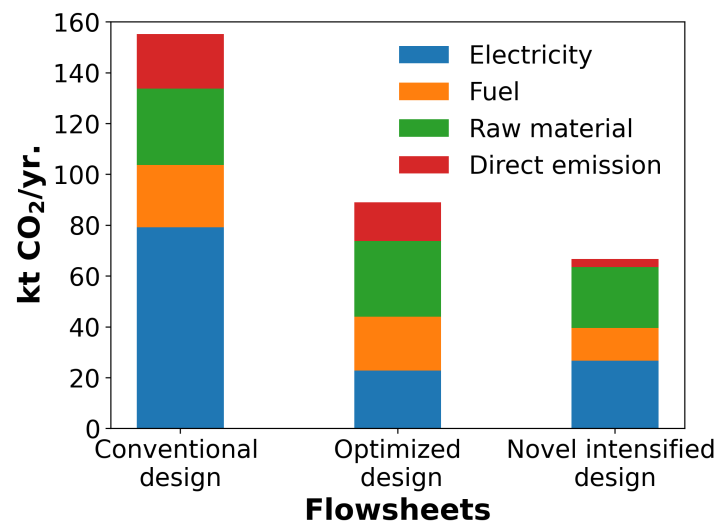
Figure 9: Comparison of CO₂-equivalent emissions.

Table 1: Capital cost parameters and scaling factors.

Equipment	Reference installation cost C_e (MM\$)	Scaling factor n_e	Reference size S_e^{ref}	Scaling parameter S_e	Reference year
POX reactor[56]	67.24	0.67	15199	Flow rate (MSCFH)	2009
WGS reactor[70]	7.29	0.67	150	Feed flow rate (kg s^{-1})	2016
MeOH reactor[71]	19.05	0.6	87.5	Feed flow rate (kg s^{-1})	2006
VLE separator[71]	2.86×10^{-3}	0.8	1	Feed flow rate (kg s^{-1})	2000
Heater, cooler, and heat exchanger[71]	69.02	1	355	Heat duty (MW)	2007
Compressor[71]	24.52	0.67	10	Power requirement (MW)	2006
CO_2 membrane separator[72]	5×10^{-5}	1	1	Membrane area (m^2)	2008
POX membrane[73]	0.13	1	560	Membrane area (m^2)	-
MeOH membrane[74]	8×10^{-4}	1	1	Membrane area (m^2)	2001
Distillation column[73]	1.15	0.53	100	Height $\times$ diameter$^{1.5}$ (m$^{2.5}$)	-
Distillation trays[73]	6.3×10^{-3}	0.8	2.13	Diameter (m)	-

Table 2: Economics and sustainability of the process flowsheets.

Flowsheets	Conventional design	Optimized design	Novel intensified design
AI (MM\$/yr)	65.9	68.6	75.6
AOC (MM\$/yr)	40.6	36.0	30.7
Natural gas (MM\$/yr)	16.9	16.9	16.9
Oxygen (MM\$/yr)	12.7	12.5	8.4
Steam (MM\$/yr)	0.04	0.01	0.1
Hot utility (MM\$/yr)	2.4	2.1	1.4
Cold utility (MM\$/yr)	3.5	3.0	2.2
Electricity (MM\$/yr)	5.1	1.5	1.7
FCI (MM\$)	80.5	58.4	63.0
POX reactor (MM\$)	20.1	20.0	20.9
POX membrane (MM\$)	-	-	0.1
WGS reactor (MM\$)	1.2	1.2	-
MeOH reactor (MM\$)	7.6	7.2	10.4
MeOH membrane (MM\$)	-	-	0.2
VLE separators (MM\$)	0.09	0.09	0.1
Coolers (MM\$)	9.2	6.9	3.0
Heaters (MM\$)	2.6	2.1	-
Heat exchangers (MM\$)	0.6	0.5	6.1
Compressors (MM\$)	33.3	14.5	16.1
CO_2 separator (MM\$)	0.02	0.02	-
Distillation column (MM\$)	5.8	5.9	6.1
Annualized FCI (MM\$/yr)	9.5	6.8	7.4
AMC (MM\$/yr.)	4.0	2.9	3.1
TAC (MM\$/yr)	54.1	45.7	41.2
TAP (MM\$/yr)	11.8	22.9	34.4
ROI (%/yr)	18.2	32.8	42.0
e^{CO_2} (kt CO_2/yr)	155.3	89.0	66.7